Color-dependent interactions in the three coloring model

Philipp C. Verpoort,[1,2] Jacob Simmons,[3] and Claudio Castelnovo[1,4,5]
[1]*Department of Physics, University of Cambridge, J.J. Thomson Avenue, Cambridge CB3 0HE, United Kingdom*
[2]*Karlsruhe Institute of Technology, Institute for Theory of Condensed Matter, D-76131 Karlsruhe, Germany*
[3]*James Franck Institute, University of Chicago, Chicago, Illinois 60637, United States*
[4]*Rudolf Peierls Centre for Theoretical Physics, University of Oxford, Oxford OX1 3NP, United Kingdom*
[5]*SEPnet and Hubbard Theory Consortium, Department of Physics, Royal Holloway University of London, Egham TW20 0EX, United Kingdom*

(Received 23 February 2018; published 3 July 2018)

Since it was first discussed by Baxter in 1970, the three coloring model has been studied in several contexts, from frustrated magnetism to superconducting devices and glassiness. In presence of interactions, when the model is no longer exactly soluble, it was already observed that the phase diagram is highly nontrivial. Here we discuss the generic case of "color-dependent" nearest-neighbor interactions between the vertex chiralities. We uncover different critical regimes merging into one another: $c = 1/2$ free fermions combining into $c = 1$ free bosons; $c = 1$ free bosons combining into $c = 2$ critical loop models; as well as three separate $c = 1/2$ critical lines merging at a supersymmetric $c = 3/2$ critical point. When the three coupling constants are tuned to equal one another, transfer-matrix calculations highlight a puzzling regime where the central charge appears to vary continuously from $3/2$ to 2.

DOI: 10.1103/PhysRevB.98.024403

I. INTRODUCTION

The three coloring model was introduced by Baxter in 1970 as the combinatorial problem to compute the "number of ways. . . of coloring the bonds of a hexagonal lattice. . . with three colors so that no adjacent bonds are colored alike." The author showed that the model is integrable in the absence of interactions and proceeded to find an exact solution [1].

In the absence of interactions, a parallel can be drawn between the three coloring model and the fully packed loop model with fugacity 2. The latter is critical and was argued to have central charge $c = 2$ and SU(3) symmetry by Reshetikhin [2], from results on the integrability of the model. At a kagome workshop in 1992, N. Read presented a formulation of the model that illustrates explicitly the SU(3) symmetry and argued that the long-wavelength limit is described by an $SU(3)_1$ conformal field theory [3], by means of mapping to a two-component height model [4]. This was later confirmed by Kondev and collaborators [5].

The model received renewed attention when it was noticed that three coloring configurations describe the ground states of a Heisenberg antiferromagnet on the kagome lattice [4]. The physics of the three coloring model was also found to be relevant to the behavior of arrays of Josephson junctions [6,7] and kagome networks of superconducting wires [7–10], provided that appropriate (uniform) interactions are introduced in the model. These interactions—which are typically written in terms of vertex chirality spins, encoding the parity of the three colors that appear around each vertex—were shown to give rise to an exotic thermodynamic behavior, encompassing lines of critical points with varying critical exponents [7]. The interplay between interactions and coloring constraints gives rise to a novel type of dynamical obstruction to equilibration whereby the system freezes into a polycrystal instead of reaching its ordered ground state [7,11–13].

Here we study the effects of nearest-neighbor interactions where the interaction strength depends on the color of the intervening bond between the two neighboring vertices (color-dependent interactions). We show that this leads to an unusually rich phase diagram with different ordered phases separated by lines, sheets and even three-dimensional regions of critical points (in parameter space). In particular, the ability to tune the interaction according to the color of the bond that "carries" it allows us to *break down* the criticality with central charge $c = 2$ of the noninteracting model and to see it *arise from its originating components*, all the way down to three Ising $c = 1/2$ critical points.

Along the symmetric line, where the three coupling constants are equal, we observe a line of critical points whose central charge appears (numerically) to be varying from $c = 2$ to $c = 3/2$, as first noted in Ref. [14] (Fig. 4). Whilst our work allows to understand the origin of the value $c = 3/2$, the behavior of the system in between the two points remains a mystery—plausibly the effect of some unusually large but not critical correlation length which tricks here (and nowhere else in the phase diagram) the numerical algorithms into measuring an incorrect value of the central charge.

The paper is organized as follows. In Sec. II A, we introduce the model and we present a summary of our main results with an overview of the complete phase diagram of the model. The remaining sections are an account of the analytical calculations, arguments, and numerics that support our results. In Sec. III, we study some useful limits, where analytical progress can be made by mapping to other known models, and we compare our findings to numerical results from transfer-matrix calculations. In Sec. IV, we apply the transfer-matrix method to the rest of the phase diagram of the system. This section contains the most important results in the paper: the $c = 2$ criticality can be viewed as arising from the merging of $c = 1$ free-boson planes

of critical points, which in turn originate each by the merging of two $c = 1/2$ planes of critical points. We argue that the model exhibits a (seemingly supersymmetric) $c = 3/2$ critical point where three Ising $c = 1/2$ critical planes merge. And we also observe a region where the central charge appears to be varying continuously between $3/2$ and 2 as a function of the coupling constants—a likely artifact of an unusually large but finite correlation length whose origin is yet to be fully understood. Finally, we draw our conclusions in Sec. V.

Details of the transfer-matrix calculations are given in Appendix A. For completeness, we provide details of Read's argument for the $SU(3)_1$ CFT description of the noninteracting three coloring model in Appendix B.

II. MODEL AND SUMMARY OF RESULTS

A. Model

Consider a honeycomb lattice with degrees of freedom living on the bonds and taking three different values, or colors, A, B, and C, under the constraint that no two bonds meeting at a vertex can be of the same color. Each vertex on the lattice must then be in one of the configurations illustrated in Fig. 1, up to cyclic rotations of the colors.

In the noninteracting limit, i.e., from a purely combinatorial perspective, the model is exactly soluble and it exhibits long range correlations [2]. As it was elegantly shown by N. Read at a kagome workshop in 1992, the discrete $\mathcal{S}_3$ symmetry of the system is promoted to a continuous SU(3) symmetry of the coarse grained CFT describing its long wavelength behavior (see Appendix B).

The model can be alternatively interpreted as a fully packed loop model with fugacity 2. For instance, removing all bonds of a given color, say C, from the lattice yields a fully packed configuration of closed loops with alternating coloring AB or BA. This in turn allows one to map the three coloring model onto a two-component height model, which in the noninteracting limit is sitting precisely at a roughening transition [5]. Note that one is free to choose a description in terms of AB, BC, or CA loops: any three coloring configuration can indeed be seen as the classical superposition of three coexisting fully packed loop configurations (strongly correlated with one another!).

One can introduce chirality spins $\sigma_i = \pm 1$ on the sites of the honeycomb lattice, the positive sign assigned say to vertices where the colors appear counterclockwise in an even permutation of the sequence ABC (as illustrated in Fig. 1). The three coloring model can then be mapped onto a constrained Ising system on the sites of a honeycomb lattice, where each plaquette has either magnetization 0 or ± 6. [7]

The effect of nearest-neighbor interactions between the spins was studied in Ref. [7] by a combination of numerical and analytical techniques (see also Ref. [14] for further results). The behavior is surprisingly rich, as highlighted for example by the fact that weak antiferromagnetic (AFM) interactions do not seem to order the system, but rather give rise to a mysterious line of critical points with an apparent 'continuously' varying central charge [14]. This is surprising, given the fact that the system is at a roughening transition in the noninteracting limit, precisely towards the AFM phase, and the addition of AFM interactions should give a finite mass to the critical modes. Moreover, a continuously varying central charge is forbidden by Zamolodchikov's c theorem in unitary theories; following the general belief that a model with local constraints and real local energy terms is unitary.

Partly in the attempt to shed light into this unusual behavior, we consider a generalization of the model in this paper. We assume that the strength of the nearest-neighbor couplings between the Ising spins depends on the color of the intervening bond, and the interaction energy is given by

$$E = -\sum_{l=A,B,C} J_l \sum_{\langle ij\rangle_l} \sigma_i \sigma_j, \tag{2.1}$$

where $\langle ij\rangle_l$ stands for a pair of neighboring sites i, j connect by a bond of color $l \in \{A, B, C\}$. We investigate the phase diagram of the system as a function of the reduced couplings J_l/T with T being temperature, and for convenience of notation we shall directly use the relabeling

$$J_A \equiv \frac{J_A}{T}, \quad J_B \equiv \frac{J_B}{T}, \quad J_C \equiv \frac{J_C}{T}. \tag{2.2}$$

The phase space is spanned by the three real coordinates $J_l \in (-\infty, \infty)$, which we compactify for convenience to $(-1, +1)$ by introducing the parameters

$$x_l = \tanh J_l\,, \qquad \text{with } l = A, B, C\,. \tag{2.3}$$

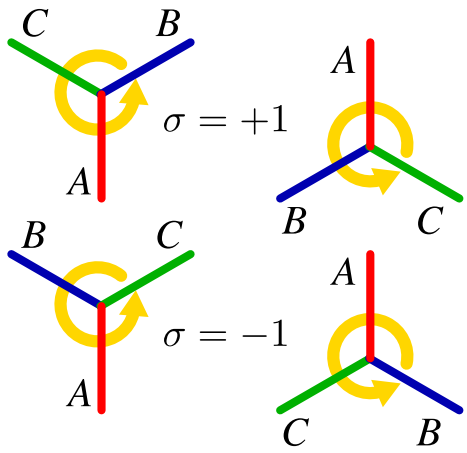

FIG. 1. Allowed vertices in the three coloring model (modulo cyclic rotations of the colors) and relative values of the chirality spins (namely, the parity of the color sequence around the vertex in the counterclockwise direction). [A bonds are red, B bonds are blue, and C bonds are green throughout the rest of this paper.]

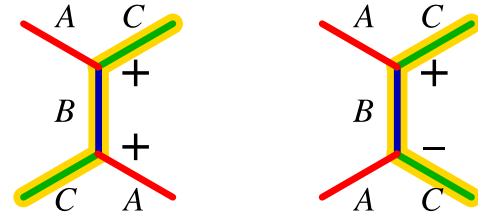

FIG. 2. A FM arrangement of the chirality spins (left) say across a B bond minimizes the local energy for $x_B > 0$ and corresponds to configuring the adjacent A and C bonds parallel colorwise. This results in "straight" AB and BC loop segments. Vice versa for an AFM arrangement of spins (right).

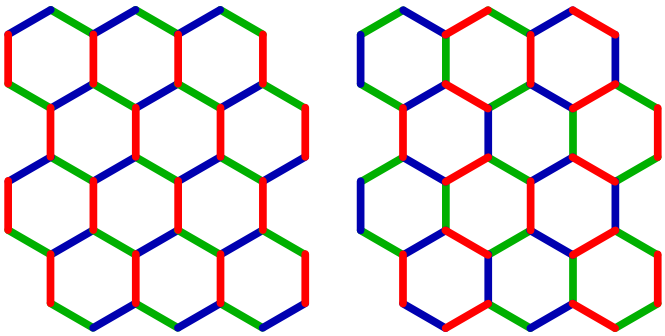

FIG. 3. Examples of fully ferromagnetic (left) and antiferromagnetic (right) coloring configurations.

The Boltzmann weight for bond k, which connects neighboring vertices i and j, can then be rewritten as

$$e^{J_{l_k}\sigma_i\sigma_j} = e^{J_{l_k}}\delta_{\sigma_i\sigma_j,+1} + e^{-J_{l_k}}\delta_{\sigma_i\sigma_j,-1} \tag{2.4}$$

$$= \cosh(J_{l_k})\big(1 + x_{l_k}\,\sigma_i\sigma_j\big), \tag{2.5}$$

where l_k is the color of bond k. The factor of $\cosh(J_{l_k})$ can be neglected, since it contributes a trivial overall factor to the partition function.

A positive (ferromagnetic, FM) coupling $x_l > 0$ favors parallel bonds of the same color, as illustrated in Fig. 2. As such, it favors straight loop configurations (i.e., it favors maximal local tilt of the height mapping in the direction of the bond). Vice versa, a negative (antiferromagnetic, AFM) coupling $x_l < 0$ favors nonparallel arrangements of colored bonds and curled loop configurations (i.e., favors locally flat configurations: if crossing a loop changes the height, crossing an adjacent loop in the same direction leads to the opposite height change). See Fig. 3 for examples of fully FM and fully AFM configurations (interactions in dimerlike models that act as loop tension—equivalently, aligning / antialigning terms—have been considered before on experimentally relevant grounds, e.g., in Ref. [15]).

B. Summary of results

For convenience, we summarize here the results of the paper, which make up the phase diagram of the system illustrated in Fig. 4. For large AFM couplings, $x_A, x_B, x_C \to -1$, the system orders in a sixfold degenerate state where all two-color loops are maximally curled into single hexagons (Fig. 3, right panel). We find a cube-shaped region whose phase is continuously connected to this fully AFM state (also referred to as the columnar phase). As we explain below, this phase breaks both lattice translation symmetry and $\mathbb{Z}_2$ symmetry. It can be seen as the FM-ordered phase of three distinct effective Ising plaquette spins, according to whether we identify the spins with the orientation of the AB, BC, or CA loops. Upon increasing either the x_A, x_B, or x_C coupling, the system eventually exits the columnar phase into three distinct paramagnetic phases where the $\mathbb{Z}_2$ symmetry is restored, but the sublattice symmetry remains broken. The corresponding phase transition is of the Ising universality class ($c = 1/2$, shown in purple in Fig. 4). These three phases correspond to disordered Ising phases, but the curled loops live (predominantly) on one of the three

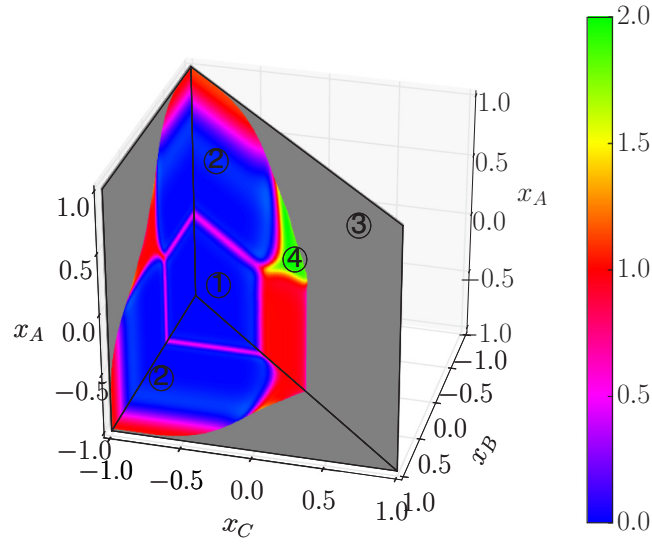

FIG. 4. The two plots of the central charge from Figs. 7 and 12 assembled on a cube. The color scale for the central charge is shown on the right, and the gray coloring indicates non-critical regions of propagating color loops. The following regions are highlighted in this plot: (1) FM-ordered Ising plaquette spin phase with broken sublattice and $\mathbb{Z}_2$ symmetry, also referred to as columnar phase; (2) paramagnetic Ising plaquette spin phase with broken sublattice but restored $\mathbb{Z}_2$ symmetry; (3) noncritical stripe phases, also referred to as staggered phases; and (4) $c = 2$ critical region containing the noninteracting limit.

different sublattices of the triangular lattice, face-dual to the original honeycomb lattice, and they appear to be nowhere continuously connected with one another in the phase diagram.

When the Ising critical boundaries from different effective descriptions merge pairwise, our numerics suggest that the $c = 1/2$ critical degrees of freedom fuse to give a $c = 1$ free-boson theory at its BKT transition [16,17]. Perhaps even more surprisingly (given that the three Ising descriptions are in fact not at all independent!), when all three $c = 1/2$ merge at the isotropic $x_A = x_B = x_C$ line, the system exhibits a $c = 3/2$ critical behavior suggestive of a supersymmetric point (confirming and providing a deeper understanding of, the results already obtained in Ref. [7,14] along the line $x_A = x_B = x_C$).

At the phase boundaries where these phases meet *pairwise*, the system becomes critical with central charge $c = 1$ (red regions in Fig. 4). As the couplings become larger, these $c = 1$ sheets develop into thick "wings" of critical points, of which we currently lack analytical understanding. The larger the value of the coupling, the thicker the wings.

Beyond the $c = 1$ wings, the system enters four different stripe-ordered phases, which are also referred to as propagating phases, as all two-color loops of bonds propagate across the entire system and do not form closed loops (shown in gray in Fig. 4). One of the four phases is the phase with all bonds being FM aligned, shown in Fig. 3, and it is favored when all coupling constants are strongly FM. The other three phases have either all A, all B, or all C bonds AFM aligned, and they appear when respectively $x_A < 0$, $x_B < 0$, or $x_C < 0$ while the other two coupling constants are strongly FM. An example of

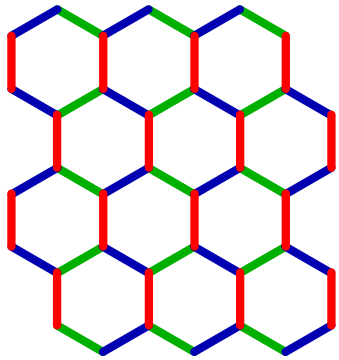

FIG. 5. Example of a configuration that minimizes the energy of the system for $x_A \to -1$, $x_C \to +1$.

such an ordered configuration is shown in Fig. 5. As discussed in Sec. III B, we expect these four phases to be stable not only in the limit of infinite coupling strength, but also in a finite region of the phase diagram. The transition between the fully FM and the three AFM phases is described by a 1D Ising model with nearest-neighbor interactions whose strength scales with the size of the system (see Sec. III F). Hence the transitions between these different stripe phases is strongly first order, as is the transition between the stripe phases and the phases that break sublattice symmetry. In the following sections, we present how these results were obtained using a combination of analytics and numerics.

III. USEFUL LIMITS

Let us begin our study of the compactified phase diagram of the model by considering some informative limiting cases.

A. The $x_A, x_B \to -1$ line

Consider the limit $x_A = x_B \to -1$, which forces the AB loops to be maximally curled around single hexagonal plaquettes (see Fig. 6), as a function of $x_C \in (-1,+1)$ (i.e., along one edge of the compactified phase diagram, see Figs. 4 and 7). The centers of the hexagonal plaquettes on the honeycomb lattice form a triangular lattice that is tripartite. Once all the AB loops

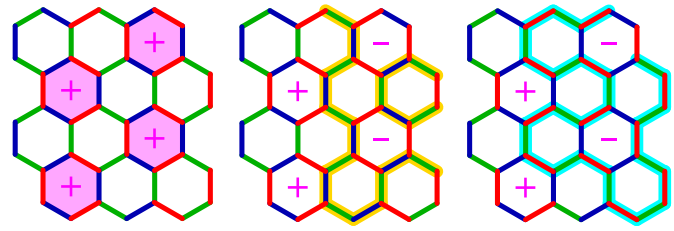

FIG. 6. Three coloring configurations with $x_A = x_B \to -1$. The effective Ising degrees of freedom live at the centers of a triangular lattice formed by one sublattice of the hexagonal plaquettes. (These are *not* to be confused with the chirality spins introduced earlier.) The left panel shows one of the two configurations that are selected in the limit $x_C \to -1$. Here we take the one illustrated as the reference configuration, where all the effective spins are positive. The middle and right panels show the same color configuration that differs from the left panel by two effective spins that have been flipped. Not all hexagonal plaquettes now form two-color loops and longer loops are present, highlighted in yellow and cyan, respectively. By comparing the panels, one can explicitly see how the x_C interaction in the effective spin language translates into a nearest-neighbor coupling of strength $-x_C$ between the plaquette spins, where the sign accounts for the fact that $x_C < 0$ is now FM.

form single hexagons, they are bound to occupy exclusively one of the three sublattices. In the limit $x_A = x_B \to -1$, the only freedom left in coloring the system is the orientation of each hexagonal AB loop, say from $ABABAB$ to $BABABA$, which does not change the sublattice of the dual triangular lattice occupied by the AB loops. As a result, this phase breaks lattice translation symmetry into three sectors, depending on which of the three sublattices the AB loops "condense" on.

Within each sector, all allowed configurations are identified by the orientations of the AB loops, either $ABABAB$ or $BABABA$. In the limit $x_C \to -1$, all the loops order with the same orientation, as shown in the left panel of Fig. 6. We can then take one of these two configurations as our reference and label all others in the same sector using Ising degrees of freedom living at the centers of the AB hexagonal loops (as illustrated in Fig. 6).

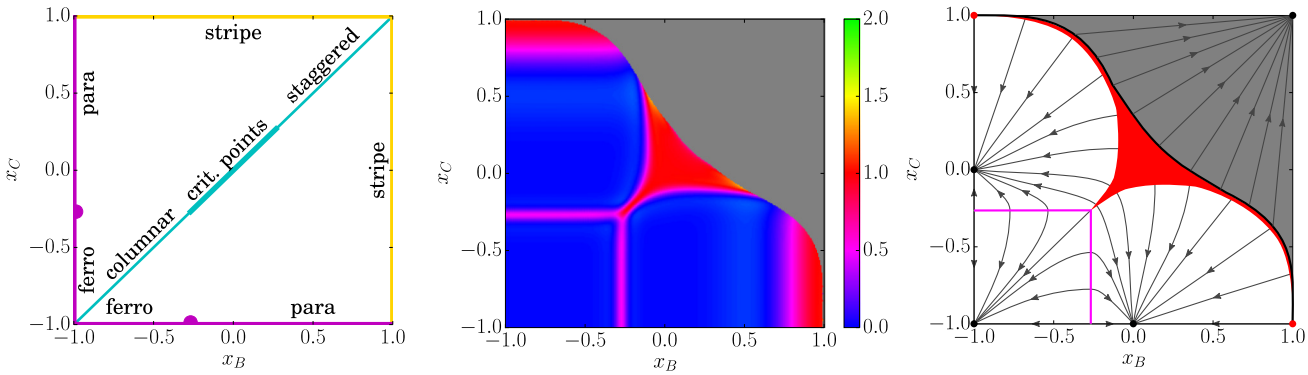

FIG. 7. (Left) Schematic illustration of the limits of the model considered in Secs. III A–III D on the $x_A \to -1$ plane. (Middle) Intensity plot of the central charge $c(x_B, x_C)$ from numerical simulations on the $x_A \to -1$ plane. The color scale for the central charge values is on the right. Lattices of size $N = 18, 24, 30$ were used to obtain these data. (Right) Schematic renormalization group flow lines for the $x_A \to -1$ plane. Note that RG flow lines have to protrude from critical lines or regions in a perpendicular way.

Namely, we can define Ising spins $S_p \in \{+1,-1\}$ at the centers p of the AB plaquettes, where $S_p = +1$ ($S_p = -1$) if the AB hexagon at p has the same (resp. different) color orientation as in Fig. 6 (left panel). What we obtain is a 1-to-1 mapping, modulo the choice of orientation of one AB plaquette, between the three coloring model in the limit of $x_A = x_B \to -1$ and a triangular lattice Ising model [18]. With the help of Fig. 6, one can verify that a finite coupling x_C translates into a nearest-neighbor interaction between the effective spins S_p,

$$E = J_C \sum_{\langle pq \rangle} S_p S_q \,. \tag{3.1}$$

Note that $x_C < 0$ is *FM* and $x_C > 0$ is *AFM* (opposite to the behavior in terms of chirality spins).

Taking advantage of the (exact) mapping in the limit $x_A,x_B \to -1$, we obtain immediately the behavior of the three coloring model as a function of x_C. Starting from the $x_C \to -1$ limit, the system is in a FM ordered phase, ending at a second-order phase transition of the Ising universality class (central charge $c = 1/2$) at $x_C^* \simeq -0.26795$ ($J_C^* \simeq -0.27465$) [19]. For larger values of x_C, the system enters a disordered phase controlled by the paramagnetic fixed point $x_C = 0$. (Note that only the $\mathbb{Z}_2$ symmetry is restored at this transition, whereas the lattice translation symmetry remains broken.)

At $x_C = 0$, positive and negative S_p spins are distributed randomly with probability $1/2$ and the model is equivalent to critical site percolation on the triangular lattice. As a manifestation of the O(1) loop model, this is part of the dense $c = 0$ phase. It is interesting to see how this single O(1) loop model originates from the three coexisting fully packed loop models (AB, BC, and CA) that identify a three coloring configuration (recall Sec. II A). Consider either the ensemble of BC or CA loops on the lattice (we shall see that the two structures give in the end the same coarse grained loop model). When three neighboring effective spins S_p have the same sign, the corresponding AB hexagons have all the same orientation and the hexagonal plaquette in the middle of the three spins must have alternating coloring, either BC or CA (see Fig. 6). By construction, this plaquette sits in the bulk of a domain of the effective Ising model. Since in site percolation one is interested in the domain boundaries, we shall remove this single BC or CA hexagon from the corresponding BC or CA loop ensemble, without losing any information. After repeating this operation throughout the lattice, we are left with BC and CA loop configurations that are no longer fully packed. One can further verify that for every loop in the former, there is a unique loop in the latter having precisely the same backbone (see the yellow and cyan shaded loops in Fig. 6) and vice versa. In other words, the two-loop configurations are effectively identical and they trace the domain walls in the S_p Ising model. These are nothing but the conventional O(1) domain wall loops in the loop gas construction by Nienhuis [20] and the critical (site percolation) behavior can be directly inferred from them.

When $x_C > 0$, the interactions between the effective spins become AFM and the model is frustrated. The disordered phase survives for any finite positive x_C, and $x_C = 0$ is the fixed point for the entire $x_C^* < x_C < +1$ basin. Spatial correlations diverge again in the limit $x_C \to +1$, where the system is equivalent to the zero-temperature limit of the classical Ising AFM on the triangular lattice. This fully frustrated system can be mapped onto a dimer model on the dual honeycomb lattice (which is *not* the same as the original lattice of the three coloring model), whose long wavelength behavior is captured by a free-boson CFT with central charge $c = 1$.

Notice that the fully frustrated triangular Ising model is only obtained if the limit $x_C \to +1$ is taken *after* $x_A,x_B \to -1$. In Sec. III B, we shall see how an entirely different behavior arises if for instance we take the limit $x_A \to -1$ first, then $x_C \to +1$ and then $x_B \to -1$. We postpone the discussion of this issue of order of limits to Sec III C.

Notice that the system is generically symmetric under any permutation of the colors and the considerations in this section extend straightforwardly to the lines $x_B = x_C \to -1$ and $x_A = x_C \to -1$ in the phase diagram. Similarly for results presented in the following sections. The results of this section are reported in the left panel of Fig. 7 in magenta.

B. The $x_A \to -1, x_C \to +1$ line

Let us consider then the other distinct edge of the back plane $x_A \to -1$ in parameter space (Fig. 4, and also Fig. 7), namely, the limit $x_A \to -1$, $x_C \to +1$ (equivalently, $x_A \to -1$, $x_B \to +1$).

It is convenient to start by setting $x_B = 0$. The energy of the system is then minimized by configurations where all A bonds are AFM ordered and all C bonds are FM ordered. These conditions can be satisfied throughout the lattice without frustration, and six configurations are selected, related by symmetry to the one shown in Fig. 5.

In these configurations, all BC loops are straight (i.e., the chirality spins are FM ordered along the loops) and there are perfect AFM correlations across the loops. Notice that all of the configurations are necessarily FM ordered across the B bonds, even in the absence of x_B interactions: the very same phase is obtained upon taking $x_B \to +1$ and $x_C \to +1$, and then taking $x_A \to -1$. In the chirality spin language, this constitutes a *stripe phase*.

Clearly, these remain the lowest (free) energy configurations for $0 < x_B < +1$. They in fact remain the lowest energy configurations in the entire region of phase space where $x_A < 0$ and $x_B,x_C > 0$. However, they have no entropy and one would need to assess whether they are stable in presence of thermal fluctuations. In analogy with previously studied dimer/loop models with tension [15,21], it is reasonable to envision that the stripe phase ($x_A \to -1$, $x_B \geqslant 0$, and $x_C \to +1$) survives in a finite 3D region of the phase diagram and is not lost as soon as the reduced couplings become finite. Indeed, one can (qualitatively) view $x_A < 0$ and $x_B,x_C > 0$ as tension terms in a fully packed BC loop model on the honeycomb lattice. The latter is expected to enter the staggered phase where all the loops are completely straight at some finite value of the reduced tension.

The case of a $-1 < x_B < 0$ tends to destabilize the stripe phase. However, this is unlikely to occur abruptly and the phase should survive a finite extent into the phase diagram for large but finite values of x_C.

Notice the peculiar entropic behavior of these ordered configurations. As one can directly verify in Fig. 5, they do not allow finite energy fluctuations. All the two-color loops wind

around the system. Consequently, the smallest re-arrangement that is obtained by exchanging the colors along one of the loops has an energy cost that scales with the linear size L of the system, whereas the entropic gain scales only as $\ln(L)$. All fluctuations about these configurations are infinitely suppressed in the thermodynamic limit: they form vanishing entropy basins in the free energy landscape of the three coloring model. We expect the system to enter or exit this phase via a first-order transition. The results of this section are reported in the left panel of Fig. 7 in yellow.

C. Noncommuting order of limits in the $(-1,-1,+1)$ corner

Notice that the behavior of the system near each of the three corners $(-1,-1,+1)$, $(-1,+1,-1)$, and $(+1,-1,-1)$ in parameter space depends on the direction of approach. Consider for instance the case $x_A = -1$. If you first take $x_C \to +1$ and then $x_B \to -1$, the system is locked into one of the 6 stripe configurations discussed in Sec. III B. On the other hand, if you first take $x_B \to -\infty$ and then $x_C \to +1$ you enter the fully frustrated limit (dual to a triangular Ising AFM) discussed in Sec. III A.

The two phases are not continuously connected and the order of limits matters. In the neighborhood of $(-1,-1,+1)$, the frustrated phase has lower energy and finite entropy, and we expect it to dominate in parameter space. This is indeed reflected in the numerical results in Sec. III E.

D. The $x_A \to -1$, $x_B = x_C$ line

Along the diagonal $x_B = x_C$ of the $x_A \to -1$ plane (see Fig. 7), it is convenient to describe the system as a BC loop model. One can verify that it is always possible to color *any* fully packed loop configuration on the honeycomb lattice so that the chirality spins are *AFM correlated across all of the bonds that are not part of the loop configuration* [22]. Indeed, there are precisely two such coloring patterns per loop configuration. Therefore, if the noninteracting three coloring model can be viewed as a fully packed BC loop model with fugacity 2, taking the limit $x_A \to -1$ simply locks the BC loop coloring with one another and reduces the fugacity from 2 to 1. It has no effect on the choice of loop covering.

As a result, we obtain a fully packed loop model on the honeycomb lattice with fugactiy 1. The couplings $x_B = x_C$ provide a tension term acting along the loops. This model was studied by Jacobsen and Alet for $x_B = x_C < 0$ [15]. The case of both positive and negative tension, albeit on the square rather than the honeycomb lattice, was studied in Refs. [21,23,24].

The tensionless limit $x_B = x_C = 0$ is equivalent to a dimer model on the honeycomb lattice, whose long wavelength correlators are the same as in a $c = 1$ free-boson CFT. Couplings $x_B = x_C > 0$ induce a tension term that favors straight loops. This leads to a line of critical points where $c = 1$ survives up to a first-order phase transition to the 'staggered' phase at a finite value of the coupling. Similarly, on the AFM side of the interactions $x_B = x_C < 0$, except that the transition to the "columnar" phase is of the Beresinskii-Kosterlitz-Thouless kind. The results of this section are reported in the left panel of Fig. 7 in turquoise.

E. Numerical results on the $x_A \to -1$ plane

In order to complete the phase diagram of the system on the $x_A \to -1$ plane, away from the limiting cases considered above, we calculate the central charge as a function of x_B and x_C using a transfer-matrix approach. This allows to identify the phase-transition boundaries between the massive phases (where $c = 0$), and provides also an initial characterization of the critical behavior.

The transfer matrix for adjacent row colorings is constructed for a three coloring configuration on a cylinder, and the free energy in the thermodynamic limit of infinite cylinder length can be obtained from the largest eigenvalue of the matrix. Computing the reduced free-energy density f (i.e., measured per temperature and unit area) for different values of the system size along the circumference L of the cylinder, and using the relation [25]

$$f(L) = f_0 - \frac{\pi c}{6L^2}, \tag{3.2}$$

the central charge c can be determined from the finite-size scaling of the free energy, where f_0 is the infinite-size free energy of the system. When constructing the transfer matrix, we find that its eigenspaces decompose into sectors of fixed numbers of bonds of the three colors on the rows winding around the cylinder. We focus only on the sector with equal number of bonds of each color, as this sector contains all the coloring configurations with no two-color loops propagating around the cylinder or along its length. Fluctuations of the latter configurations are suppressed in the thermodynamic limit, and hence the corresponding transfer-matrix sectors will be relevant only for phases of the system that are dominated by zero-entropy configurations, similar to the ones discussed in Sec. III B. We expect those phases to be noncritical, and to be connected via first-order phase transitions. We give a detailed description of the construction of the transfer matrix, the exploitation of various symmetries, and the finite-size scaling in Appendix A.

We plot the numerical results for the central charge c as a function of x_B and x_C on the $x_A \to -1$ plane in Fig. 7 (middle), where the portion of the diagram colored in gray corresponds to the propagating phase of the system. These results are in good agreement with the analytical arguments provided in Sec. III A–III D, which are indicated in Fig. 7 (left).

A first-order phase transition line separates the propagating (gray) phases from the nonpropagating (colored) phases, and is in good agreement with the first-order transition of the loop model with tension discussed in Sec. III D, as well as with the predicted ground state for the $x_A \to -1$, $x_C \to +1$ line discussed in Sec. III B.

The locations of the $c = 1/2$ ridges for $x_C \to -1$ and $x_B \to -1$ are in excellent agreement with the value $x_B^*, x_C^* = -0.26795$, that the mapping to the triangular lattice Ising models predicts (see Sec. III A). In the corners of the plane where $x_B \to +1$, or $x_C \to -1$ respectively, the numerics indicate $c = 1$, which is also in good agreement with the dimer models on a honeycomb lattice dual to the triangular lattice of the plaquette centers that is discussed in Sec. III A. The $c = 1/2$ transition lines and the $c = 1$ critical lines are surprisingly parallel to the coordinate axes, suggesting that the softening

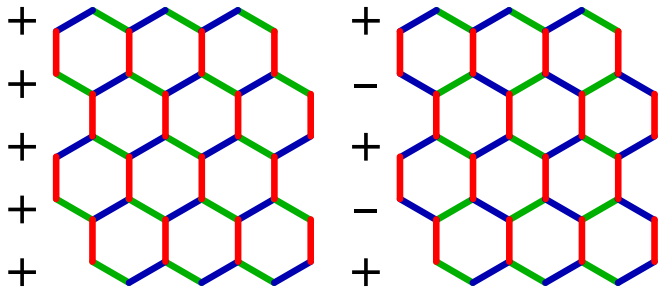

FIG. 8. Example of configurations that minimize the energy of the system for $x_B, x_C \to +1$. The left panel is favored by $x_A > 0$, the right panel by $x_A < 0$.

of the constraint that allowed the mapping to an effective Ising model does not actually alter the free energy of the latter.

The Ising $c = 1/2$ lines merge into a $c = 1$ critical point when they meet at the $x_B = x_C$ symmetry line. This appears to coincide with the end of the line of $c = 1$ critical points of the $x_B = x_C$ loop model, where it undergoes a BKT transition to the columnar phase and we can report this point to be at $x_B = x_B^*$ and $x_C = x_C^*$. A discussion of the merging of two free Majorana fermion CFTs into a free boson CFT at a BKT transition can be found in Refs. [16,17]. While the $c = 1/2$ ridges are consistent within numerical accuracy with 1D lines of critical points, the numerical results around the $c = 1 x_B = x_C$ critical line suggest that it extends into a finite 2D critical region upon increasing x_B and x_C.

We note that the numerical results cannot conclusively rule out the possibility that the $c = 1$ wings that originate from the fully packed loop model on the $x_B = x_C$ line is connected to the $c = 1$ region originating from the fully frustrated AFM on the triangular lattice in the corners of the phase diagram. This issue is discussed in further detail in Appendix A 4.

To check that the different critical behaviours observed in this model are mutually consistent, we present a plausible sketch of renormalization group (RG) flow lines on the $x_A \to -1$ plane in Fig. 7 (right). For concreteness, we consider only the case where the $c = 1$ critical regions are continuously connected.

F. The $x_B, x_C \to +1$ line

In order to investigate what happens as we leave the three 'back' planes in the phase diagram in Fig. 4, let us again consider first some limiting cases. We start here by discussing the line $x_B, x_C \to +1$ (i.e., one of the remaining independent edges of the compactified phase diagram), where the BC loops are all straight. The x_A interaction couples the coloring patterns in neighboring BC loops, so that two adjacent loops arranged as in the left panel of Fig. 8 have energy $\propto -J_A L$, whilst two adjacent loops arranged as in the right panel of Fig. 8 have energy $\propto +J_A L$, where L is the linear size of the system (in the horizontal direction in Fig. 8) and we recall that $J_A = \operatorname{artanh}(x_A)$. We assume here for simplicity a square system of size $L \times L$.

The system behaves as a classical 1D Ising chain of length L, where the Ising degrees of freedom correspond to the coloring sequence of each BC loop (either $BCBCBC\ldots$ or $CBCBCB\ldots$). In this language, J_A gives rise to a nearest neighbor interaction of effective strength $\propto J_A L/2$. Customarily, a 1D Ising model with short range interactions does not order at finite values of the couplings. However, in this case the induced coupling is proportional to the length L of the system, and hence it orders FM (AFM) for any $x_A > 0$ ($x_A < 0$). Indeed, neglecting the constant contribution due to x_B and x_C, the free energy of the system is given by

$$\begin{aligned} F &\sim -J_A L^2\,, & J_A &< 0,\\ F &\sim \ln\left(2^L\right) = \ln(2) L\,, & J_A &= 0,\\ F &\sim +J_A L^2\,, & J_A &> 0. \end{aligned} \tag{3.3}$$

In analogy with the discussion in Sec. III B, both phases ($x_A < 0$ and $x_A > 0$) are zero entropy basins of the free energy. Any transition into and out of these phases is therefore expected to be strongly first order.

G. The $x_B = x_C = 0$ line

Consider then the line where $x_B = x_C = 0$, as a function of x_A. Similarly to the discussion in Sec. III D, the behavior of the system is most readily understood if we interpret it as a fully packed loop model of BC loops. The fact that $x_B = x_C = 0$ means that there is no loop tension and the remaining interaction x_A couples the coloring patterns ($BCBCBC\ldots$ or $CBCBCB\ldots$) on adjacent loops.

In the limit $x_A \to -1$, the loops lock into an AFM pattern (i.e., the chirality spins have perfect AFM correlations *between loops*). As already mentioned in Sec. III D, one can verify that such correlations are never frustrated. That is, it is always possible to minimize each and every x_A interaction by choosing an appropriate coloring pattern for *any* chosen loop configuration [22]. In this limit, one recovers the fully packed loop model on the honeycomb lattice with fugacity 1, which is critical with central charge $c = 1$.

The noninteracting $x_A = 0$ point is a fully packed loop model with fugacity 2 (i.e., we are free to choose either the $BCBCBC\ldots$ or the $CBCBCB\ldots$ coloring for each loop). This is again critical, with central charge $c = 2$. One expects the system to simply transition from one critical theory to the other as a function of $x_A < 0$ and this is indeed confirmed numerically (see Fig. 9). However, a rigorous analytical argument to capture the transition is not readily available.

The case $x_A > 0$ is intrinsically different, since in the limit $x_A \to +1$ the system becomes "frustrated": most BC loop configurations do not allow for a coloring that produces FM correlations across all A bonds. A large positive x_A progressively selects configurations that are compatible with FM order between loops. This is a subextensive set of all configurations (there are $\sim 2^L$ of them), characterized by having all BC loops winding and parallel to each other (notice that they need not be straight, hence their number scales with 2^L). They correspond clearly to a noncritical, massive phase ($c = 0$).

Again, there is no available analytical argument to understand the transition from the $c = 2$ critical theory at $x_A = 0$ and the massive phase that obtains for $x_A \to +1$. Numerical transfer-matrix results below indicate that it happens at a finite value of $x_A > 0$ and the essentially staggered nature of the ordered phase suggests that the transition ought to be first order.

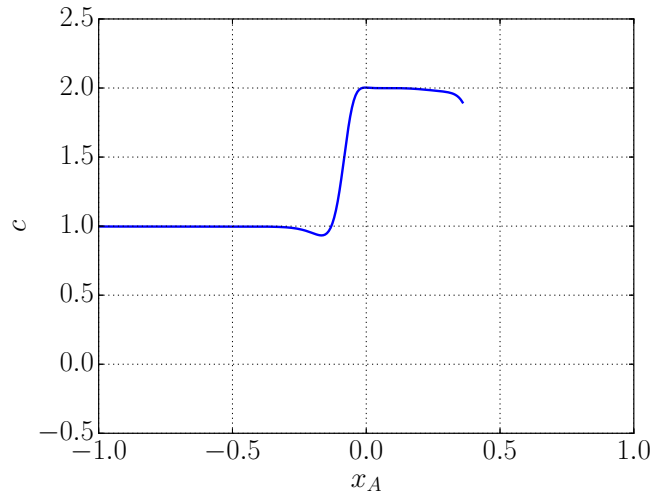

FIG. 9. Behavior of the central charge of the system along the line $x_B = x_C = 0$, as a function of x_A.

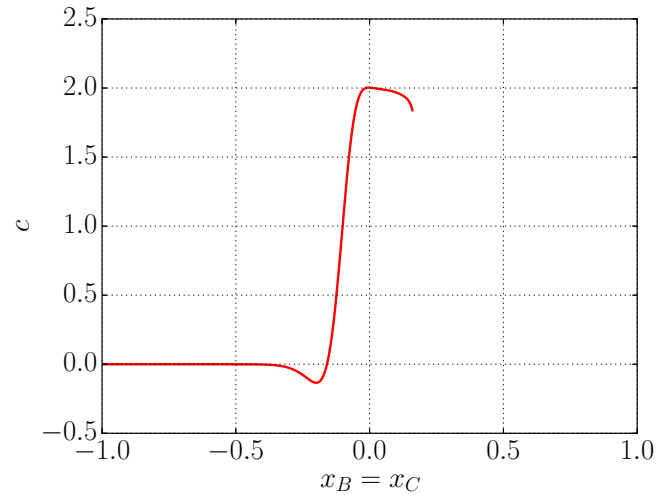

FIG. 10. Behavior of the central charge of the system along the line $x_A = 0$, $x_B = x_C = x'$.

H. The $x_A = 0$, $x_B = x_C$ line

Once again, along the line $x_A = 0$ as a function of $x_B = x_C = x'$, it is convenient to view the system as a fully packed loop model of BC loops. The loops are not interacting across A bonds. On the other hand, the coupling x' translates into a tension term along the loops (compare with the discussion in Sec. III D).

In the limit $x' \to +1$, the loops are forced to be as straight as possible, with a residual 2^L degeneracy due to the fact that each loop can be colored either $BCBCBC\ldots$ or $CBCBCB\ldots$, irrespectively of its neighbors (see Sec. III F). Vice versa, for $x' \to -1$, the loops are curled into single hexagons, with the same residual degeneracy as that of an Ising paramagnet on the triangular lattice, as discussed in Sec. III A.

The noninteracting $x' = 0$ point is a fully packed loop model with fugacity 2, which is critical with central charge $c = 2$. In analogy with the behavior of the case with fugacity 1 as a function of tension (see Sec. III D and Refs. [15,21,23,24]), one expects the system to exhibit a line of $c = 2$ critical points that terminates into a BKT transition towards the columnar phase and into a first-order transition towards the staggered phase. This is indeed consistent with the behavior of the central charge that is obtained from transfer-matrix calculations, illustrated in Fig. 10.

I. The isotropic line: $x_A = x_B = x_C$

We finally consider the phase diagram in the isotropic limit of this model ($x_A = x_B = x_C \equiv x$), which was already studied in detail in Refs. [7,14], using both numerical (transfer-matrix and Monte Carlo simulations) as well as analytical (cluster mean-field) techniques. We briefly summarize it here for completeness.

Consistently with the discussion above, the system enters a "columnar" phase for $x \to -1$. Each two-color loop is maximally curved around single hexagonal plaquettes (AFM state). Vice versa, for $x \to 1$, the system enters a "staggered" phase where all the loops are maximally straight and wind around the system (FM state).

In between these two phases, the system exhibits a line of critical points, ending in a continuous transition towards the columnar phase and in a strongly first order transition towards the staggered phase. As observed previously [14], we find a remarkably small change with system size in the central charge between the $c = 2$ and $c = 3/2$ points, in contrast to the far more substantial drift outside this range (see Fig. 11). We shall discuss this behavior in greater detail in Secs. IV and in V.

IV. THE FULL PHASE DIAGRAM

To complete the picture, we use the numerical transfer-matrix approach to study other 2D slices through the 3D phase diagram. In Fig. 12, we show the central charge values on the plane $(x_A, x_B = x_C)$ that interpolates between the $\mathbb{Z}_2$ Ising

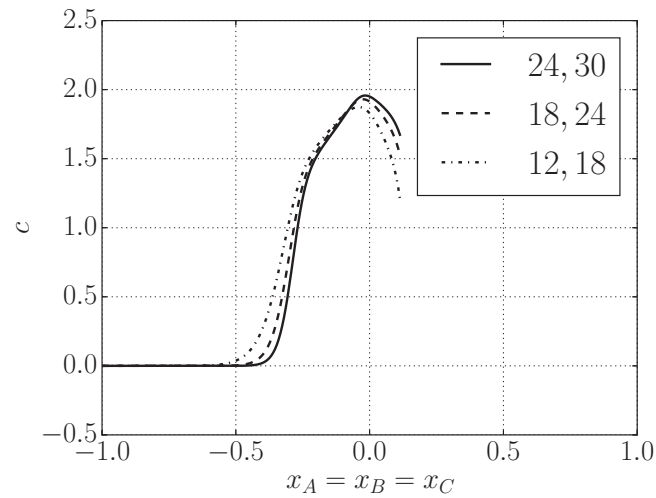

FIG. 11. Behavior of the central charge of the system along the line $x_A = x_B = x_C$. The central charge is obtained from finite-size fittings of the free energy for systems with system size N equal to (1) 30 and 24, (2) 24 and 18, and (3) 18 and 12. Notice the significantly reduced finite size change of the central charge between $c = 2$ and $c = 3/2$ (on the negative side of the horizontal axis), with respect to the behavior outside this range.

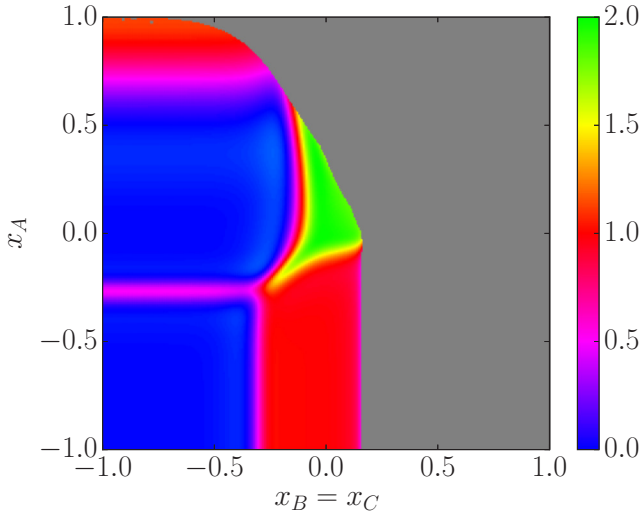

FIG. 12. Plot of $c(x_A, x_B = x_C)$ from numerical simulation on the $x_B = x_C$ plane. Lattices of size $N = 12, 18, 24$ were used to obtain this data. The color scale for the central charge values is on the right.

effective description (left vertical axis) and the fully packed loop model with tension (bottom horizontal axis). This allows us to understand that the $c = 1$ free boson line on the horizontal axis, extends into a region for finite (negative) values of x_A.

We also note that the $c = 1/2$ lines seen in Fig. 7 extend in fact to 2D $c = 1/2$ planar sheets forming three adjacent faces of the approximate cube containing the columnar ordered phase. The horizontal $c = 1/2$ line in Fig. 12 runs along the diagonal of one such cubic face. When the cubic faces meet, two distinct $c = 1/2$ critical degrees of freedom merge into a $c = 1$ BKT edge, bordering the $c = 1$ sheets discussed above. This is precisely what happens along the vertical left-most edge of the $c = 1$ sheet in Fig. 12.

Comparing these results with cuts across planes perpendicular to the isotropic $x_A = x_B = x_C$ axis, shown in Fig. 13, we see that when the three $c = 1$ sheets merge at a point $x_A = x_B = x_C \simeq -0.25$, they give rise to a region with apparent "smoothly increasing" central charge. This region starts from $c = 3/2$ at the point where the three $\mathbb{Z}_2$ Ising critical points merge—suggestive of supersymmetric properties—and increases up to $c = 2$ at approximately $x = 0$.

For positive values of the couplings, the $c = 1$ sheets develop into thick wing-shaped regions (see Fig. 7 in Sec. III E). From Figs. 12 and 13, we learn that, as these wings merge in the bulk of the phase diagram, they give rise to an extended 3D region with central charge $c = 2$, inclusive of the exactly solvable noninteracting point $x_A = x_B = x_C = 0$.

Once again, the gray regions in Figs. 12 and 13 correspond to stripe and staggered (i.e., FM) phases, as discussed in Sec. III E. The numerical results along the edges of the gray regions are consistent with the conjectured first-order nature of the transition.

V. CONCLUSIONS

We already summarized our main results and the phase diagram of the system in Sec. II B. The most controversial and interesting behavior occurs when the three sublattice-translation

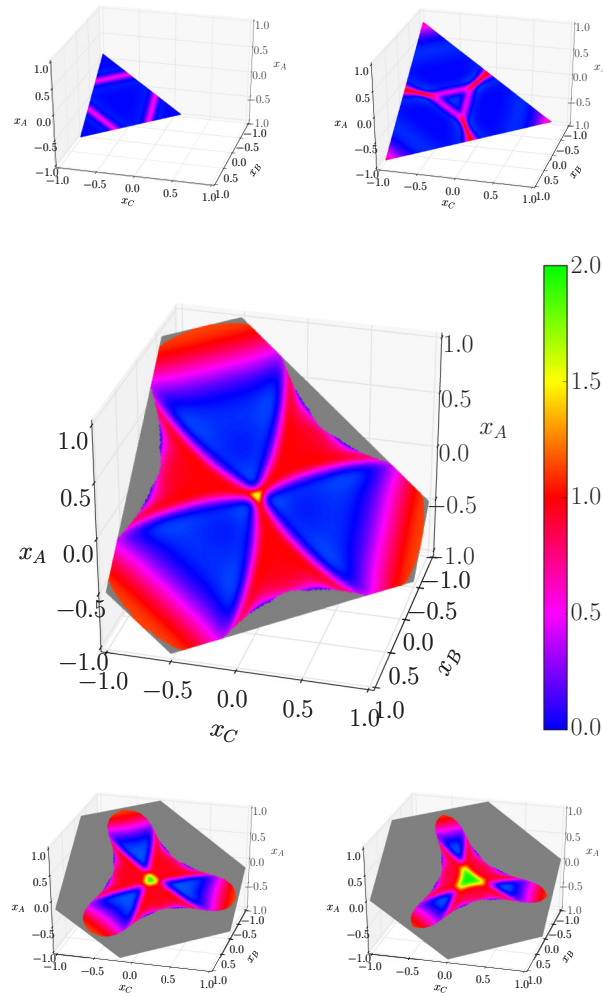

FIG. 13. Plots of c from numerical simulation on planes perpendicular to the $x_A = x_B = x_C$ line. Planes with distance -1.1, -0.7, -0.3, -0.1, and 0.0 from the origin are shown. Lattices of size $N = 12, 18, 24$ were used to obtain this data. The color scale for the central charge values is on the right.

symmetry-broken phases meet along the isotropic line $x_A = x_B = x_C \lesssim 0$. Here, the three different $c = 1$ free-boson sheets meet but their critical behavior cannot add up (as is the case instead for the $c = 1/2$ sheets meeting at the $c = 3/2$ point) because they are effective descriptions of a model that can host at most two free bosonic degrees of freedom and not three.

The result is a puzzling (numerical) central charge, which starts from $c = 3/2$ at a finite $x < 0$ and appears to increase continuously—to the best of our finite size scaling—up to $c = 2$ (see Fig. 11). However, the c-theorem forbids a continuously varying central charge along a line of fixed points in a unitary CFT.

In the study of the full phase diagram of the interacting three coloring model, we have seen how one can sometimes map the system onto a fully packed loop model with different values of the fugacity. Interestingly, if the fugacity is varied continuously between 1 and 2 in such a model, unitarity is lost and the system remains critical in between the two unitary limits, with a continuously varying central charge between 1 and 2 [26]. One may therefore wonder whether the interacting

three coloring model may in fact be nonunitary. However, the fact that the constraints are local and the interactions are real and local suggest otherwise, and we cannot offer a convincing argument in favor of nonunitarity. An alternative intriguing conjecture is that the RG flow lines of the unitary three coloring model along the $x_A = x_B = x_C$ line may run close to those of a nonunitary fully packed loop model with continuously varying fugacity, thence exhibiting its scaling behavior up to very large length scales (beyond which the true scaling of the unitary model would be reveled—length scales which are unfortunately not accessible using our numerical transfer-matrix approach). What the true unitary behavior of the system is in between the $c = 3/2$ and $c = 2$ points remains therefore elusive: one possible scenario is that the central charge remains constant at $3/2$ up to the $x_A = x_B = x_C \sim 0$ point, where it increases to 2; the difference between the two CFTs is a massive versus massless Majorana fermion, which may be responsible for an unusually long correlation length that is mistakenly picked up by the finite-size scaling as an effective contribution to the central charge. However, one can clearly envisage many alternative scenarios and further work is needed to fully elucidate this conundrum. The software to generate the numerical values for the central charge, the data obtained from it for the cases studied and plotted in this paper, and the scripts to generate those plots from the data are available online [27].

ACKNOWLEDGMENTS

This work spurred from a collaboration with C. Mudry and C. Chamon, and the authors are deeply indebted to them, for several of the ideas regarding the isotropic limit of the model developed from those early discussions. Since its inception in 2005, several collaborators joined and left this project, with noteworthy contributions from F. Trusselet and P. Pujol. We are particularly grateful to Nick Read for sharing his private notes written at a kagome workshop in 1992, and for taking the time to discuss them with us in detail. Part of those notes are reproduced with his permission in Appendix B of this manuscript. We are indebted to J. Cardy for several insightful discussions and for pointing out the c-theorem argument against a continuously varying central charge in Sec. V. Furthermore, P. Verpoort thanks V. Jouffrey, M. J. Rutter, and B. Andrews for helpful discussions concerning the numerical calculations. This work was supported in part by Engineering and Physical Sciences Research Council (EPSRC) Grant No. GR/R83712/01 and by EPSRC Postdoctoral Research Fellowship EP/G049394/1 (C. Castelnovo), and by EPSRC Grant No. EP/D070643/1 (JJHS). P. Verpoort acknowledges funding by the Studienstiftung des deutschen Volkes. Statement of compliance with the EPSRC policy framework on research data: this publication reports theoretical work that does not require supporting research data.

APPENDIX A: DETAILS OF THE TRANSFER-MATRIX CALCULATIONS

We begin by considering a cylindrical lattice of circumference L with N bonds and infinite length, as illustrated in Fig. 14. We label the coloring configurations of each horizontal

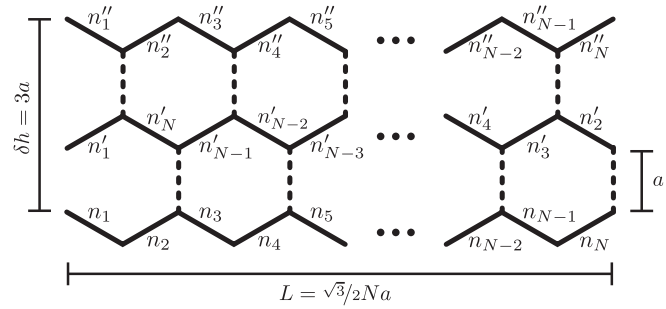

FIG. 14. Bond labels used in the transfer-matrix approach. Measurements are given relative to the edge length a.

row of the system by $n,n',n'',\ldots \in \mathcal{B}$, where we use the basis set $\mathcal{B} = \{n \in (A,B,C)^N : n_i \neq n_{i+1}\}$, and we apply periodic boundary conditions $n_i = n_{i+N}$.

The transfer matrix is a matrix with elements $T_{n,n''}$ that vanish identically if the stacking of n and n'' is not an allowed three coloring configuration, and that take the value of the sum of the contributions to the Boltzmann factor of all the bonds on n and between n and n'' for an allowed stacking. With this well-known prescription, the partition function of the system can be obtained as $Z(L) = \lim_{k\to\infty} \mathrm{Tr}(T^k)$, from which we can derive $f(L) = -\lim_{k\to\infty}[\ln \mathrm{Tr}(T^k)]/(LK)$, where $K = k \times \delta h$ is the length of the cylinder, and δh is defined in Fig. 14. If T has a unique largest eigenvalue Λ_0^T, then $f(L) = -\ln \Lambda_0^T/(L\delta h)$.

With the current choice of orientation, it is clear that the transfer matrix has geometrically inequivalent indices: row n is not related to row n' by a mere vertical translation, which is why we have so far only defined the transfer matrix T to act between next-nearest neighboring rows n and n''. T is the standard transfer matrix, and it is positive semidefinite and symmetric. Here, we choose to proceed by decomposing T into the product of two semitransfer matrices τ, which then act between nearest-neighboring rows n and n'. We adopt the labeling scheme shown in Fig. 14, which treats nearest-neighboring rows differently. This convention implies that $\sum_{n'} \tau_{n\,n'}\tau_{n'\,n''} = T_{n\,n''}$. The largest eigenvalue Λ_0^T of matrix T is then equal [28] to the square of the largest eigenvalue Λ_0^τ of matrix τ, i.e., we find $\Lambda_0^T = (\Lambda_0^\tau)^2$. Therefore by setting the edge length $a = 1$, we find the following relation between the largest eigenvalue of τ and the finite-size scaling with bond number N,

$$-\frac{2\sqrt{3}}{\pi}\frac{\ln\,\Lambda_0^\tau}{N} = \gamma_0 - \frac{c}{N^2}\,, \tag{A1}$$

where γ_0 is the fitting parameter for the free-energy of the infinite-size system.

For convenience, we write the semitransfer matrix as

$$\tau_{n\,n'} = \rho(n)\,\omega(n,n')\,, \tag{A2}$$

where $\rho(n)$ accounts for all the Boltzmann weights of the bonds on the horizontal row n, and $\omega(n,n')$ accounts for all the weights of the vertical bonds connecting rows n and n' (where the numbering according to Fig. 14 is used, and $\omega(n,n') = 0$ for

nonmatching n and n'). Using Eq. (2.5), this can be written as

$$\rho(n) = \prod_{i=1}^{N} \left[1 - (-1)^{\delta_{n_{i-1}n_{i+1}}} x_{n_i}\right], \tag{A3}$$

where $(-1)^{\delta_{n_{i-1}n_{i+1}}} = \pm 1$ if the colors on the bonds $i-1$ and $i+1$ are different (equal), corresponding to an AFM (FM) contribution of the interaction term across bond i. Note that we are not checking the validity of the color configuration n because it is inherently chosen from the set of allowed row colorings $\mathcal{B}$. Similarly, we can write

$$\omega(n,n') = \prod_{\substack{j=2 \\ \text{(even)}}}^{N} \left[\delta_{n_j n'_{N-j+1}} \delta_{n_{j+1} n'_{N-j+2}} \left(1 + x_{\ell_{n_j,n_{j+1}}}\right) + \delta_{n_j n'_{N-j+2}} \delta_{n_{j+1} n'_{N-j+1}} \left(1 - x_{\ell_{n_j,n_{j+1}}}\right)\right], \tag{A4}$$

where we introduced the index $\ell_{n_j,n_{j+1}} \in \{A,B,C\}$ such that $n_j \neq \ell_{n_j,n_{j+1}} \neq n_{j+1}$ (recall that n_j and n_{j+1} are different by definition). The function $\omega(n,n')$ simultaneously checks that the two row configurations match one another respecting the color constraints at all vertices (via the product of delta functions), and contributes to the corresponding Boltzmann factor.

1. Coloring-sector decomposition and nonpropagating sector

Consider two pairs of two horizontal bonds connected via a vertical bond, e.g., (n_{2m},n_{2m+1}) and $(n'_{N+2-2m},n'_{N+1-2m})$ in Fig. 14. Due to the hard coloring constraint, the bonds of these two pairs must be of the same color, which in turn implies that the number of A, B, and C bonds in the basis row is conserved by the action of the transfer matrix. Thus we can decompose the transfer matrix into sectors classified by the numbers N_A, N_B, and N_C of the A, B, and C bonds respectively within the basis states.

This decomposition has important implications, which are clearest in the loop representation. Observe that each closed AB loop crossing between two adjacent rows via an A bond must either cross back via a B bond, or cross forward to the next row via an A bond, as shown in Fig. 15. All closed two-color loops contribute an equal number of bonds of each of the two colors on a row of vertical bonds. An imbalance in the number of A, B, and C vertical bonds signals the presence of propagating loops running along the length of the cylinder. The condition of equal numbers of bonds of each color on each *vertical* row of bonds is equivalent to the condition of equal numbers of bonds of each color on each *horizontal* row of bonds, i.e., $N_A = N_B = N_C$. Hence all other transfer-matrix sectors that do not satisfy that condition must contain coloring configurations with propagating two-color loops.

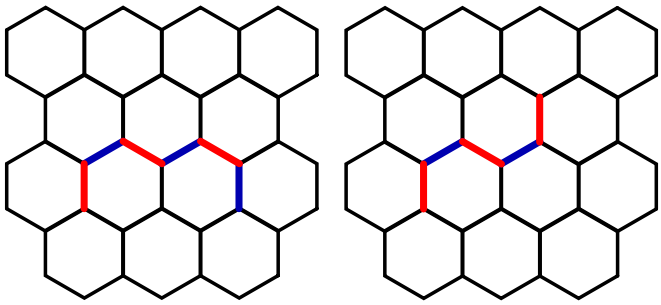

FIG. 15. After crossing between adjacent rows via a vertical bond, a loop can propagate along the row either an even number of bonds, and cross backward to the first row via a vertical bond of opposite color (left), or it can propagate an odd number of bonds, and cross forward to the next row via a vertical bond of the same color (right).

In this paper, we focus on the transfer-matrix sectors with equal number of bond colors to study the nonpropagating phase of the system. The propagating phases, where some two-color loops are extended and run either along the length of the cylinder or wind around it, have their excitations suppressed in the thermodynamic limit, and hence represent zero-entropy systems that can only be favored energetically. We therefore expect the phase transition between the propagating and the nonpropagating phases to be of first order. We do not treat those phases with the finite-size scaling approach, but instead only compute the line of first-order phase transitions between the propagating and nonpropagating phases in our simulations by comparing the largest eigenvalue of the nonpropagating transfer-matrix sector with the largest eigenvalues of all other sectors for fixed system size $N = 18$.

Finally, for systems with number of bonds on a horizontal row N being not a multiple of 6, the condition $N_A = N_B = N_C$ cannot be fulfilled and the argument presented above forces propagating loops to be present independent of the values of the coupling constants. These propagating loops appear due to geometric frustration, which does not play a role in the limit of an infinite system. Hence, we restrict N for the configurations used in the transfer-matrix and finite-size calculations to be an integer multiple of 6.

2. Proof of the irreducibility of the transfer-matrix sectors

In Sec. A 3, we will use symmetries of the semi-transfer matrix to simplify our calculations. This requires that the coloring sectors defined in Sec. A 1 are irreducible, for which we provide a proof here.

Irreducibility of each coloring sector is equivalent to the possibility to connect two given row configurations by a finite number of intermediate steps of vertical and horizontal rows, which we construct for an arbitrary row coloring below. Specifically, we prove that two adjacent vertical bonds can be interchanged by adding two rows of horizontal and one row of vertical bonds. Since that operation generates the full permutation group, this is sufficient as proof.

Start with a configuration of vertical bonds [see Fig. 16(a)], for which we intend to interchange two neighboring bonds. We assume those two bonds to be red and green (without loss of generality). Next, add a set of horizontal bonds [see Fig. 16(b)] in such a way that the two vertical bonds that we want to interchange are connected via the same colors, i.e., again red and green. The fact that this is always possible, is discussed in the next paragraph. Next, copy all the horizontal bond colorings to the next horizontal row [see Fig. 16(c)]. Finally, pick all missing bond colors to fulfill the coloring constraint [see Fig. 16(d)]. So far, the original coloring of the vertical bonds has been reproduced. Next, repeat the four steps laid out above, but this time, when copying the horizontal bond

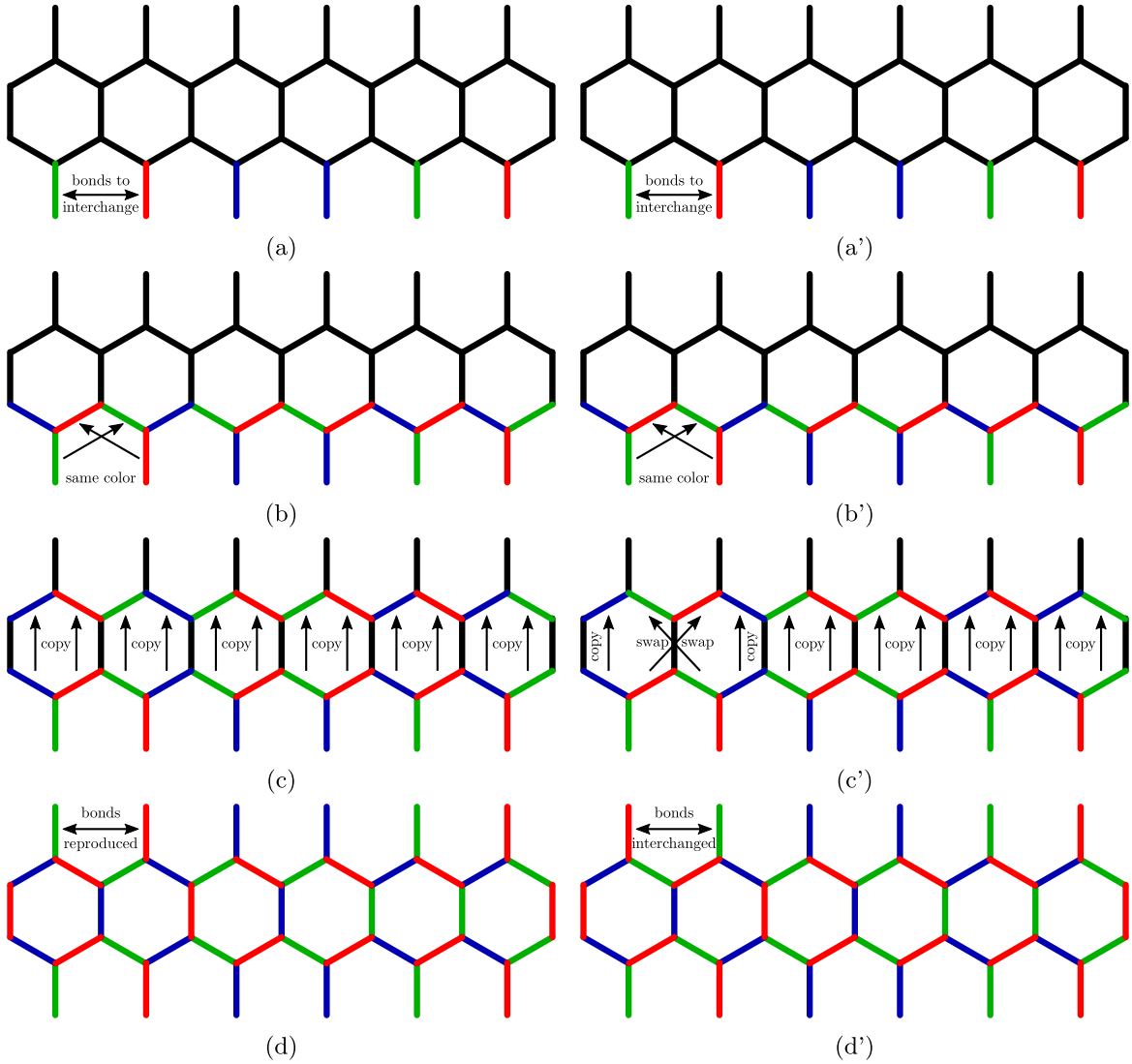

FIG. 16. Two vertical bonds can be interchanged by first reproducing the same bonds (left) and then changing the horizontal bonds between those two vertical bonds in the process (right).

colorings, swap the two horizontal bonds connected to the two vertical bonds that we intend to interchange [see Figs. 16(a') to 16(d')]. The system ends up with the desired configuration of vertical bonds, where only two adjacent vertical bonds have been interchanged.

We now have to show that it is always possible to find a horizontal row configuration that connects the two vertical bonds that we intend to interchange via the same color, i.e., red and green (see bonds in gray box in Fig. 17). This forces the next attached horizontal bond to be blue. If the next vertical bond is red (green), we are forced to continue with one green (red) and one blue bond on the horizontal row [see Figs. 17(a) and 17(b)]. However, if the next vertical bond is blue, we can choose the next two horizontal bonds to be either red and green or green and red [see Figs. 17(c) and 17(d)], and therefore the next bond can be any of the three colors, which puts no further constraint on all following bonds on the horizontal row. Thus the statement holds as long as there exists at least one vertical blue bond.

Therefore, in the case that the vertical bonds have at least one bond of each color, the sector is irreducible. This is the case when $N_A, N_B, N_C < N/2$. Otherwise, if for example $N_B = N/2$,

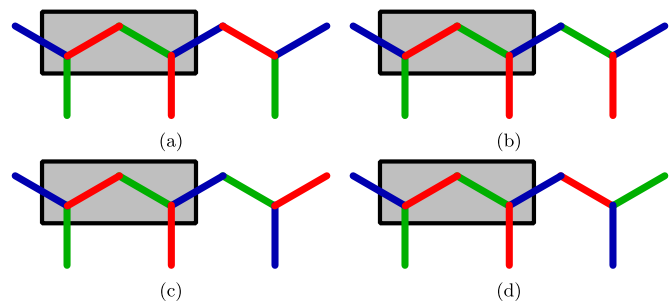

FIG. 17. To be able to interchange two adjacent vertical bonds as described in Fig. 16, they have to be connected to each other via the same colors on the horizontal row. This can always be done if there is at least one vertical bond of the other color (blue in this example).

the system is in a state in which all AC loops travel the length of the cylinder. We assume these sectors to be relevant only for the stripe phase, when it is well separated (in phase space) from the nonpropagating phases that we are focusing our studies on, and we can therefore neglect the lack of irreducibility for these sectors.

3. Transfer-matrix symmetries

The symmetry group of the lattice is generated by two discrete transformations: rotations $\mathcal{R}_\pm : n_i \to n_{i\pm2}$, and inversions $\mathcal{I}_\pm : n_i \to n_{N+2-i\mp1}$. The plus (minus) signs have to be taken when acting on the right (left) increasing states, i.e., when acting on n (n') in Fig. 14, so that τ is symmetric with respect to the symmetry transformations,

$$\tau_{n,n'} = \tau_{\mathcal{R}_+ n,\mathcal{R}_- n'} \quad \text{and} \quad \tau_{n,n'} = \tau_{\mathcal{I}_+ n,\mathcal{I}_- n'}\,. \tag{A5}$$

$\mathcal{R} \in \{\mathcal{R}_+,\mathcal{R}_-\}$ and $\mathcal{I} \in \{\mathcal{I}_+,\mathcal{I}_-\}$ generate the full group of symmetry operations $\mathcal{A}$ with N elements,

$$\begin{aligned}\mathcal{A} = \{&\mathbf{1},\mathcal{R},\mathcal{R}^2,\ldots,\mathcal{R}^{N/2-1},\\ &\mathcal{I},\mathcal{I}\mathcal{R},\mathcal{I}\mathcal{R}^2,\ldots,\mathcal{I}\mathcal{R}^{N/2-1}\}\,,\end{aligned} \tag{A6}$$

and it holds that $\mathcal{R}^{N/2} = \mathcal{I}^2 = \mathbf{1}$, and $\mathcal{R}\mathcal{I}\mathcal{R} = \mathcal{I}$.

If τ was invariant under symmetry operations acting equally on its two indices, the matrix would naturally decouple into momentum and parity eigenstates. This is not the case here, as for example τ couples states of opposite momenta, which is clear from $\tau_{n,n'} = \tau_{\mathcal{R}_+ n,\mathcal{R}_- n'}$. However, the zero momentum eigensectors still decouple, as we show hereafter.

We define $n_{rv} = \mathcal{R}_+^r \mathcal{I}_+^v n_0$ for a fixed $n_0 \in \mathcal{B}$ with $r = 0,1,2,\ldots,q-1$, and $v = 0,1$, where q is half the length of the shortest repeating sequence of n_0. Analogously, we define $n'_{r'v'}$, and therefore write the elements of τ as $\tau_{rv,r'v'} = \tau_{n_{rv},n_{r'v'}}$. The rotational symmetry of τ takes the form

$$\tau_{rv,r'v'} = \tau_{rv,(-r+r+r')v'} = \tau_{0v,(r+r')v'} = \tau_{v,v'}(r+r')\,, \tag{A7}$$

and the inversion symmetry takes the form

$$\begin{aligned}\tau_{v+1,v'+1}(r+r') &\overset{(A7)}{=} \tau_{0(v+1),(r+r')(v'+1)}\\ &\overset{\text{def.}}{=} \tau_{\mathcal{I}_+^{v+1} n_0,\mathcal{R}_+^{r+r'}\mathcal{I}_+^{v'+1} n_0} = \tau_{\mathcal{I}_+\mathcal{I}_+^v n_0,\mathcal{R}_+^{r+r'}\mathcal{I}_+\mathcal{I}_+^{v'} n_0}\\ &\overset{(A5)}{=} \tau_{\mathcal{I}_+^v n_0,\mathcal{I}_-\mathcal{R}_+^{r+r'}\mathcal{I}_+\mathcal{I}_+^{v'} n_0} \overset{(*)}{=} \tau_{\mathcal{I}_+^v n_0,\mathcal{I}_+\mathcal{R}_+^{r+r'-1}\mathcal{I}_+\mathcal{I}_+^{v'} n_0}\\ &\overset{(**)}{=} \tau_{\mathcal{I}_+^v n_0,\mathcal{R}_+^{-r-r'+1}\mathcal{I}_+^{v'} n_0} = \tau_{v,v'}(-r-r'+1),\end{aligned} \tag{A8}$$

where we used that $\mathcal{I}_- = \mathcal{I}_+\mathcal{R}_+^{-1}$ $(*)$ and $\mathcal{I}\mathcal{R}\mathcal{I} = \mathcal{R}^{-1}$ $(**)$. The transformation into moment and parity eigenstates,

$$v_{k\sigma} = \sum_{r\,v} e^{ikr} e^{i\sigma v} n_{rv}\,, \tag{A9}$$

then yields the matrix element,

$$\begin{aligned}\tau_{k\sigma,k'\sigma'} &= \sum_{r\,r'}\sum_{v\,v'} e^{-i(kr-k'r')} e^{-i(\sigma v-\sigma' v')}\tau_{rv,r'v'}\\ &\overset{(A7)}{=} \delta_{k,-k'}\sum_{r''} e^{-ikr''}\sum_{v\,v'} e^{-i(\sigma v-\sigma' v')}\tau_{vv'}(r''),\end{aligned} \tag{A10}$$

where we mapped $r \mapsto r + r' = r''$. Hence the matrix only couples states of opposite momenta to each other. In particular, the zero-momentum sector decouples from all other sectors. For $k = k' = 0$, it further holds that

$$\begin{aligned}\tau_{k\sigma,k'\sigma'} &= \sum_{r''}\sum_{v\,v'} e^{-i(\sigma v-\sigma' v')}\tau_{vv'}(r'')\\ &= \sum_{r''}\sum_{v} e^{-iv(\sigma-\sigma')}[\tau_{vv}(r'') + e^{i\sigma'}\tau_{v(v+1)}(r'')],\end{aligned} \tag{A11}$$

and by using the inversion symmetry of τ [see Eq. (A8)] and letting $r'' \to -r'' + 1$ in the term with $v = 1$,

$$\begin{aligned}\tau_{k\sigma,k'\sigma'} &= 2\sum_{r''}\sum_{v} e^{-iv(\sigma-\sigma')}[\tau_{00}(r'') + e^{i\sigma'}\tau_{01}(r'')]\\ &= \delta_{\sigma\sigma'} 2\sum_{r''}[\tau_{00}(r'') + e^{i\sigma'}\tau_{01}(r'')].\end{aligned} \tag{A12}$$

Thus also the parity eigensectors decouple.

This result can also be obtained more intuitively by realizing that a symmetric state $v_0 = v_{k=0,\sigma=0}$ is invariant under symmetry transformations. It holds that $\mathcal{R}_- v_0 = \mathcal{R}_+ v_0$ and $\mathcal{I}_- v_0 = \mathcal{I}_+ v_0$. The symmetry relation for τ in Eq. (A5) then becomes

$$\tau_{v,v'} = \tau_{\mathcal{R}_+ v,\mathcal{R}_+ v'} \quad \text{and} \quad \tau_{v,v'} = \tau_{\mathcal{I}_+ v,\mathcal{I}_+ v'}\,, \tag{A13}$$

as long as one of v or v' is in the zero-momentum and zero-parity eigensector. The result then follows from standard Fourier and parity-eigenstate transformations.

The fact that the zero-momentum eigensector decouples from all other sectors of the semi-transfer matrix is important, since it contains the eigenvector corresponding to the largest eigenvalue. To understand this, let v be an eigenvector of the semitransfer matrix τ with eigenvalue λ. A fully symmetric vector can be defined by

$$v_{\text{sym}} = \sum_{\mathcal{Q}\in\mathcal{A}} \mathcal{Q} v, \tag{A14}$$

which is equally an eigenvector of τ with eigenvalue λ. This new eigenvector could in principle be zero. Since T is nonnegative and each coloring sector is irreducible (see Appendix A 2), the Perron-Frobenius theorem insures that all components of the eigenvector corresponding to the largest eigenvalue are strictly positive. If v is positive (i.e., all its components are positive), then so must be the components of the transformed eigenvectors $\mathcal{Q}v$ with $\mathcal{Q} \in \mathcal{A}$. Therefore, if λ is the largest eigenvalue, the symmetric summation in Eq. (A14) has to be nonzero. Thus, for the largest eigenvalue, there exists at least one eigenvector that is symmetric under all symmetry transformations $\mathcal{Q} \in \mathcal{A}$ of the semitransfer matrix τ.

We proceed by transforming τ into the basis of fully symmetric vectors. All other sectors can be neglected, since the symmetric sector contains the largest eigenvalue. For each subspace that is spanned by the M elements of a symmetry class $[n] = \{\tilde{n} : \exists\mathcal{Q} \in \mathcal{A} \text{ so that } \tilde{n} = \mathcal{Q}n\}$, the following matrix of dimension $M \times M$ defines a valid similarity transformation,

$$U = \left(\begin{array}{c|ccc} 1 & 1 & \cdots & 1\\ \hline 0 & & & \\ \vdots & & \mathbb{1} & \\ 0 & & & \end{array}\right), \quad U^{-1} = \left(\begin{array}{c|ccc} 1 & -1 & \cdots & -1\\ \hline 0 & & & \\ \vdots & & \mathbb{1} & \\ 0 & & & \end{array}\right).$$

Looking at only the first component of this transformed subspace, which represents the fully symmetric superposition, it holds that

$$\tau_{[n],[n']} = [n]U\tau U^{-1}[n'] = \sum_{s\in[n]} \tau_{s,n'}. \tag{A15}$$

Thus, to obtain the matrix element between the symmetric superpositions of any two symmetry classes $[n]$ and $[n']$, we compute the individual matrix element of each s in the symmetry class $[n]$ with an arbitrary but fixed element n' of class $[n']$, and sum up all these individual matrix elements. The spectrum of the matrix remains the same under the similarity transformation. Therefore the largest eigenvalue of τ is the same as the largest eigenvalue of the matrix in the symmetrized basis.

4. Fitting of finite-size effects

As explained in the main text, our numerical results are built upon the finite-size scaling of the reduced free-energy density in Eq. (A1). This scaling relation holds when mapping the CFT describing the long-wavelength limit of an infinite system onto a cylinder. In our simulations, we are only able to access systems of relatively small size with respect to the lattice spacing. This introduces additional finite-size effects, which we expect to fade away as $N \to \infty$. In order to account for this, it is customary to add further terms to the fitting formula,

$$-\frac{2\sqrt{3}}{\pi}\frac{\ln\Lambda_0^\tau}{N} = \gamma_0 - \frac{c}{N^2} + \frac{\gamma_3}{N^3} + \frac{\gamma_4}{N^4} + \cdots. \tag{A16}$$

We find that our final results depend slightly on what additional fitting terms we include. In Fig. 18, we present the numerical results of the central charge for the $x_A \to -1$ plane (compare to Fig. 7) that we obtain by either omitting all optimization parameters other than γ_0 and c, or by using γ_4 as an additional fitting parameter, where we set the number of different system sizes N used equal to the number of optimization parameters. (Adding γ_3 or other higher-order fitting terms results in very poor data with unphysical values of the central charge, and we therefore do not present it here.)

The additional fitting terms introduce errors, i.e., some slight unphysical negative values for the central charge. However, they also make transitions between different values of the central charge sharper. In the paper we decided to fit the free energy using the optimization with parameters γ_0, c, and γ_4.

It is worth mentioning that the data obtained from fits without any additional optimization parameters ($\gamma_4 = 0$) suggests that the $c = 1$ wings originating from the fully packed loop model on the $x_B = x_C$ line (see Sec. III A) are connected to the $c = 1$ region originating from the fully frustrated AFM on the triangular lattice in the corners of the phase diagram (see Sec. III D). This is in contrast to the case when γ_4 is also used. For a conclusive answer on this matter, more extensive numerical calculations are in order, which is beyond the scope of this paper.

Finally, it is important to mention that the numerical results on the $x_A \to -1$ plane can achieve a higher accuracy than in the rest of the phase diagram, since all matrix elements with FM A bonds vanish in this limit. This allows us to significantly reduce the size of the transfer matrix, and therefore reach larger system sizes with N up to 30.

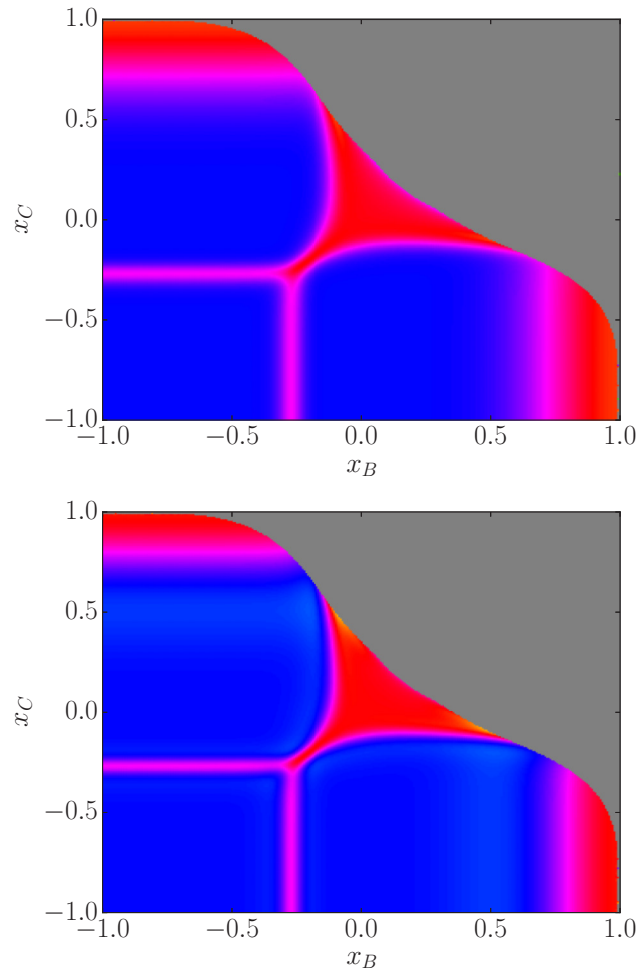

FIG. 18. (Top) Results for the central charge for fitting it with the CFT finite-size scaling using only c and γ_0 as fitting parameters. (Bottom) The same results using γ_4 as an additional fitting parameter. Lattices of size up to $N = 30$ were used to obtain these data. For the color coding, see Fig. 7. Gray regions have been confirmed to have the largest eigenvalue in one of the propagating transfer-matrix sectors.

APPENDIX B: SU(3) SYMMETRY IN A DISCRETE $\mathcal{S}_3$ SYSTEM

At a kagome workshop in 1992, N. Read presented an argument illustrating how a continuous SU(3) symmetry can emerge from the inherent discrete $\mathcal{S}_3$ symmetry in the three coloring model. From this argument, he further obtained that the model is described in the continuum limit by an $SU(3)_1$ CFT. We believe that the argument (which was never published) can help the reader understand the behavior of this model.

The argument begins by noting the equivalence between the phase space of the three coloring model and the degenerate ground state configurations of the classical three-state Potts AFM on the kagome lattice at zero temperature. The classical partition function of the AFM three-state Potts model is

$$Z^{(3)}_{\text{Potts}}(T) = \sum_{\{\sigma_i\}} e^{-\beta H^{(3)}_{\text{Potts}}}, \tag{B1a}$$

$$H^{(3)}_{\text{Potts}} \equiv J \sum_{\langle ij\rangle} (\delta_{S_i S_j} - 1), \tag{B1b}$$

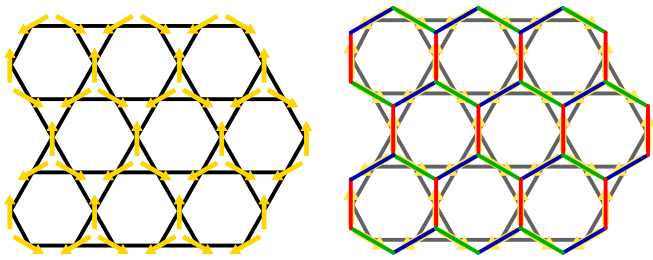

FIG. 19. Mapping of a three-state Potts model ground-state configuration onto the three coloring model. (Left) An exemplary ground-state configuration of spins in the three-state Potts model (also referred to as the all-in all-out configuration). (Right) The corresponding configuration of the three coloring model (observe that this is the fully FM configuration).

where $J > 0$, $\langle ij \rangle$ denotes directed nearest-neighbor sites on the kagome lattice, and the three-state Potts variables are

$$S_i = 1,2,3\,. \tag{B1c}$$

The exchange interaction $J(\delta_{S_i S_j} - 1)$ assumes the value $-J$ when $S_i \neq S_j$ and the value 0 when $S_i = S_j$. A state with $S_i \neq S_j$ for all $\langle ij \rangle$ belongs to the ground state manifold and has energy $-JN_{\langle ij \rangle}$, where $N_{\langle ij \rangle}$ is the number of nearest-neighbor links of the kagome lattice.

At zero temperature,

$$Z^{(3)}_{\text{Potts}}(0) = \left[\lim_{\beta\to\infty} e^{\beta J N_{\langle ij \rangle}}\right] \sum_{\{\sigma_i\}} \prod_{\langle ij \rangle} (1 - \delta_{\sigma_i \sigma_j}). \tag{B2}$$

The ground-state manifold of the AFM three-state Potts model on the kagome lattice is invariant under the group $\mathcal{S}_3$ of global permutations of the values 1, 2, 3 taken by the Potts spins. One can straightforwardly find a one-to-one correspondence between this ground state manifold and the phase space of the three coloring model on the honeycomb lattice by simply drawing the (dual) hexagonal lattice joining the centers of the triangular plaquettes in the kagome lattice and identifying the colors A, B, C with the values 1, 2, 3 assumed by the Potts variables (see Fig. 19).

The argument to suggest that there exists a hidden SU(3) symmetry in the three-state Potts AFM at zero temperature is elegantly simple. First of all, let us extend the phase space allowing for color mismatches across the bonds. Each vertex has three bonds of different colors departing from it (which we call a *decorated vertex*), but now bonds connecting two spins can have two different colors at the two ends (see Fig. 20). The enlarged phase space is the one obtained by covering the honeycomb lattice with decorated vertices *independently of one another*, for a total of 6^N configurations on a honeycomb lattice of N sites.

One then assigns a three-dimensional (complex) vector

$$\boldsymbol{b}_\ell \equiv \left(b^\alpha_\ell\right) = \begin{pmatrix} b^1_\ell \\ b^2_\ell \\ b^3_\ell \end{pmatrix} \in \mathbb{C}^3 \tag{B3a}$$

to each bond ℓ of the lattice, as illustrated in Fig. 20, with the idea of identifying each color with a different component of the vector: A with the first component, B with the second, and

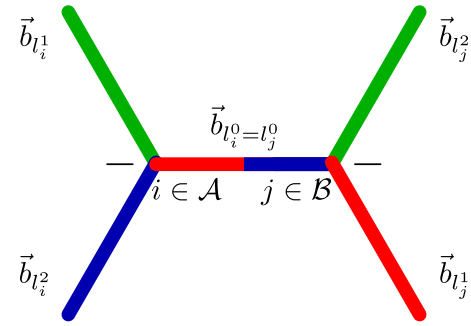

FIG. 20. Illustration of the extended phase space of the three coloring model, which allows color mismatches across the bonds.

C with the third one. Using these vectors, one can construct the following terms:

$$\sum_{\alpha_1=1}^{3}\sum_{\alpha_2=1}^{3}\sum_{\alpha_3=1}^{3} \varepsilon_{\alpha_1,\alpha_2,\alpha_3} b^{\alpha_1}_{\ell_i^1} b^{\alpha_2}_{\ell_i^2} b^{\alpha_3}_{\ell_i^3}, \tag{B3b}$$

$$\sum_{\beta_1=1}^{3}\sum_{\beta_2=1}^{3}\sum_{\beta_3=1}^{3} \varepsilon_{\beta_1,\beta_2,\beta_3} \bar{b}^{\beta_1}_{\ell_j^1} \bar{b}^{\beta_2}_{\ell_j^2} \bar{b}^{\beta_3}_{\ell_j^3} \tag{B3c}$$

associated to vertices i, j belonging to sublattice $\mathcal{A}$ and $\mathcal{B}$, respectively. Here, $\alpha_{1,2,3}$ and $\beta_{1,2,3}$ are used to index the components of vectors $\boldsymbol{b}_\ell$ and their complex conjugates $\bar{\boldsymbol{b}}_\ell$. The labels ℓ^q_i and ℓ^q_j refer to the three bonds $q = 1,2,3$ departing from vertex $i \in \mathcal{A}$ and $j \in \mathcal{B}$ respectively. This notation, though simple, is clearly redundant, as nearest neighboring sites share one bond and therefore

$$\langle i,j \rangle \;\Rightarrow\; \ell^q_i \equiv \ell^q_j, \qquad \exists!\; q = 1,2, \text{or } 3\,, \tag{B3d}$$

(see Fig. 20). Note that the Levi-Civita (totally antisymmetric) tensor,

$$\epsilon_{\alpha_1\alpha_2\alpha_3} = \begin{cases} +1 & \text{if } (\alpha_1,\alpha_2,\alpha_3) \text{ is an even} \\ & \text{permutation of } (1,2,3) \\ -1 & \text{if } (\alpha_1,\alpha_2,\alpha_3) \text{ is an odd} \\ & \text{permutation of } (1,2,3) \\ 0 & \text{otherwise} \end{cases}, \tag{B3e}$$

is used here to ensure that no two colors (A, B, $C \;\Leftrightarrow\; \alpha_1$, α_2, $\alpha_3 = 1,2,3$) are repeated at any vertex. The product of all the above terms, corresponding to all the sites of the honeycomb lattice,

$$\prod_{i\in\mathcal{A}} \left[\sum_{\alpha_1=1}^{3}\sum_{\alpha_2=1}^{3}\sum_{\alpha_3=1}^{3} \varepsilon_{\alpha_1,\alpha_2,\alpha_3} b^{\alpha_1}_{\ell_i^1} b^{\alpha_2}_{\ell_i^2} b^{\alpha_3}_{\ell_i^3}\right] \times \prod_{j\in\mathcal{B}} \left[\sum_{\beta_1=1}^{3}\sum_{\beta_2=1}^{3}\sum_{\beta_3=1}^{3} \varepsilon_{\beta_1,\beta_2,\beta_3} \bar{b}^{\beta_1}_{\ell_j^1} \bar{b}^{\beta_2}_{\ell_j^2} \bar{b}^{\beta_3}_{\ell_j^3}\right], \tag{B3f}$$

gives a sum of terms in one-to-one correspondence with all the 6^N configurations of *decorated vertices*. Each bond ℓ contributes a factor given by the product of the $\boldsymbol{b}_\ell$ components,

$$b^\alpha_\ell \bar{b}^{\alpha'}_\ell\,, \tag{B3g}$$

where α and α' are related to the colors of the bond ℓ close to its adjacent sites belonging to sublattice $\mathcal{A}$ and to sublattice $\mathcal{B}$, respectively.

Upon integration over the complex variables

$$\prod_{\alpha,\ell} db_\ell^\alpha d\bar{b}_\ell^\alpha , \tag{B4}$$

all the terms containing at least one factor (B3g) having $\alpha \neq \alpha'$ vanish because of complex phase integration. This eliminates all unwanted configurations where colors mismatch across a given bond. One can therefore construct the partition function of the original three coloring model as a sum of integrals over continuous variables. The result gives the partition function in Read's presentation at the kagome workshop:

$$\begin{aligned} Z_{\mathrm{U}(3)} = \int \prod_{\ell\in\Lambda} \prod_{\alpha_\ell=1,2,3} \frac{db_\ell^{\alpha_\ell} d\bar{b}_\ell^{\alpha_\ell}}{2\pi \mathrm{i}} \exp\left(-|b_\ell^{\alpha_\ell}|^2\right) \\ \times \prod_{i\in\mathcal{A}} \left[\sum_{\alpha_1=1}^{3} \sum_{\alpha_2=1}^{3} \sum_{\alpha_3=1}^{3} \epsilon_{\alpha_1\alpha_2\alpha_3} b_{\ell_i^1}^{\alpha_1} b_{\ell_i^2}^{\alpha_2} b_{\ell_i^3}^{\alpha_3} \right] \\ \times \prod_{j\in\mathcal{B}} \left[\sum_{\beta_1=1}^{3} \sum_{\beta_2=1}^{3} \sum_{\beta_3=1}^{3} \epsilon_{\beta_1\beta_2\beta_3} \bar{b}_{\ell_j^1}^{\beta_1} \bar{b}_{\ell_j^2}^{\beta_2} \bar{b}_{\ell_j^3}^{\beta_3} \right], \end{aligned} \tag{B5}$$

where Λ is the set of all bonds on the honeycomb lattice, and a convergence Gaussian factor $\exp(-|b_\ell^{\alpha_\ell}|^2)$ was introduced to normalize the nonvanishing integrals.

In Eq. (B5), we overlooked one important aspect: all nonvanishing terms in the partition function $Z_{\mathrm{U}(3)}$ ought to be positive, whereas the Levi-Civita tensor elements can take negative values. The sign of each term in $Z_{\mathrm{U}(3)}$ is given by the product of all elements $\varepsilon_{\alpha\beta\gamma}$ appearing in the integrand. These are nothing but the chirality spins introduced in Sec. II A, i.e., the parities of the three colors around each site of the lattice, say counterclockwise. Whereas this product is not in general positive (see for instance the recent systematic study in Ref. [29] and references therein), it is conserved by any loop updates (local or winding). Indeed, by selecting an alternating coloring path on the lattice, say $ABABAB\ldots$, and exchanging the two colors along the path $A \leftrightarrow B$, we flip all the chirality spins along the path. On a lattice with periodic boundary conditions, the number of sites along the path is *always even* (for appropriately chosen system sizes that respect sublattice symmetry as well as color tiling). Therefore, within each sector of phase space identified by configurations that are connected to one another by loop updates, we have that $Z_{\mathrm{U}(3)} = Z^{(3)}_{\mathrm{Potts}}(0)$ or $Z_{\mathrm{U}(3)} = -Z^{(3)}_{\mathrm{Potts}}(0)$, and the SU(3) symmetry argument given below holds separately in each sector.

Moreover, on appropriately commensurate lattices, one can show that the relevant ordered configurations (staggered, stripe, and columnar) discussed in the main text satisfy the condition of the product of all chirality spins being positive, and they are connected to one another via loop updates. According to Ref. [29], this sector of phase space is the largest one, and at the very least N. Read's construction applies to it.

In order to discuss the symmetries of the partition function $Z_{\mathrm{U}(3)}$, it is convenient to rewrite it as

$$\begin{aligned} Z_{\mathrm{U}(3)} &= \int \prod_{\ell\in\Lambda} \frac{d\boldsymbol{b}_\ell \cdot d\bar{\boldsymbol{b}}_\ell}{2\pi \mathrm{i}} \exp(-\bar{\boldsymbol{b}}_\ell \cdot \boldsymbol{b}_\ell) \\ &\quad \times \prod_{i\in A} \left[\boldsymbol{b}_{\ell_i^1} \cdot \left(\boldsymbol{b}_{\ell_i^2} \wedge \boldsymbol{b}_{\ell_i^3}\right)\right] \prod_{j\in B} \left[\bar{\boldsymbol{b}}_{\ell_j^1} \cdot \left(\bar{\boldsymbol{b}}_{\ell_j^2} \wedge \bar{\boldsymbol{b}}_{\ell_j^3}\right)\right] \\ &= \int \prod_{\ell\in\Lambda} \frac{d\boldsymbol{b}_\ell \cdot d\bar{\boldsymbol{b}}_\ell}{2\pi \mathrm{i}} \exp(-\bar{\boldsymbol{b}}_\ell \cdot \boldsymbol{b}_\ell) \\ &\quad \times \exp\left\{ \sum_{i\in A} \ln\left[\boldsymbol{b}_{\ell_i^1} \cdot \left(\boldsymbol{b}_{\ell_i^2} \wedge \boldsymbol{b}_{\ell_i^3}\right)\right] \right. \\ &\quad \left. + \sum_{j\in B} \ln\left[\bar{\boldsymbol{b}}_{\ell_j^1} \cdot \left(\bar{\boldsymbol{b}}_{\ell_j^2} \wedge \bar{\boldsymbol{b}}_{\ell_j^3}\right)\right] \right\}. \end{aligned} \tag{B6}$$

The second equality emphasizes the local and the three-body nature of the interaction. The symmetries of $Z_{\mathrm{U}(3)}$ are the following.

(1) Invariance under local U(1) transformations,

$$\begin{aligned} &\bar{\boldsymbol{b}}_\ell \to e^{-\mathrm{i}\theta_\ell} \bar{\boldsymbol{b}}_\ell, \qquad \boldsymbol{b}_\ell \to e^{+\mathrm{i}\theta_\ell} \boldsymbol{b}_\ell, \\ &\theta_\ell \in [0, 2\pi[\qquad \forall \ell \in \Lambda. \end{aligned} \tag{B7}$$

Note that $\boldsymbol{b}_{\ell_i^1} \cdot (\boldsymbol{b}_{\ell_i^2} \wedge \boldsymbol{b}_{\ell_i^3})$ has U(1) charge $+3$ and that $\bar{\boldsymbol{b}}_{\ell_j^1} \cdot (\bar{\boldsymbol{b}}_{\ell_j^2} \wedge \bar{\boldsymbol{b}}_{\ell_j^3})$ has U(1) charge -3.

(2) Invariance under global SU(3) transformations,

$$\begin{aligned} &\bar{\boldsymbol{b}}_\ell \to \bar{U}\, \bar{\boldsymbol{b}}_\ell, \qquad \boldsymbol{b}_\ell \to U\, \boldsymbol{b}_\ell, \\ &\forall \ell \in \Lambda \qquad U \in \mathrm{SU}(3). \end{aligned} \tag{B8}$$

Note that the measure $\prod_{\ell\in\Lambda} d\boldsymbol{b}_\ell \cdot d\bar{\boldsymbol{b}}_\ell \exp(-\boldsymbol{b}_\ell \cdot \bar{\boldsymbol{b}}_\ell)$ is invariant under local U(3) transformations

$$\begin{aligned} &\bar{\boldsymbol{b}}_\ell \to \bar{U}_\ell\, \bar{\boldsymbol{b}}_\ell, \qquad \boldsymbol{b}_\ell \to U_\ell\, \boldsymbol{b}_\ell, \\ &U_\ell \in \mathrm{U}(3), \qquad \forall \ell \in \Lambda, \end{aligned} \tag{B9}$$

whilst the integrand

$$\prod_{i\in A} \left[\boldsymbol{b}_{\ell_i^1} \cdot \left(\boldsymbol{b}_{\ell_i^2} \wedge \boldsymbol{b}_{\ell_i^3}\right)\right] \prod_{j\in B} \left[\bar{\boldsymbol{b}}_{\ell_j^1} \cdot \left(\bar{\boldsymbol{b}}_{\ell_j^2} \wedge \bar{\boldsymbol{b}}_{\ell_j^3}\right)\right] \tag{B10}$$

is invariant under local SU(3) transformations,

$$\begin{aligned} &\left(\bar{\boldsymbol{b}}_{\ell_j^1}, \bar{\boldsymbol{b}}_{\ell_j^2}, \bar{\boldsymbol{b}}_{\ell_j^3}\right) \to \bar{U}_j \left(\bar{\boldsymbol{b}}_{\ell_j^1}, \bar{\boldsymbol{b}}_{\ell_j^2}, \bar{\boldsymbol{b}}_{\ell_j^3}\right), \\ &U_j \in \mathrm{SU}(3), \qquad \forall j \in B, \end{aligned} \tag{B11a}$$

$$\begin{aligned} &\left(\boldsymbol{b}_{\ell_i^1}, \boldsymbol{b}_{\ell_i^2}, \boldsymbol{b}_{\ell_i^3}\right) \to U_i \left(\boldsymbol{b}_{\ell_i^1}, \boldsymbol{b}_{\ell_i^2}, \boldsymbol{b}_{\ell_i^3}\right), \\ &U_i \in \mathrm{SU}(3), \qquad \forall i \in A. \end{aligned} \tag{B11b}$$

(3) Invariance under a transformation that induces the local change

$$\boldsymbol{b}_{\ell_i^1} \cdot \left(\boldsymbol{b}_{\ell_i^2} \wedge \boldsymbol{b}_{\ell_i^3}\right) \to -\boldsymbol{b}_{\ell_i^1} \cdot \left(\boldsymbol{b}_{\ell_i^2} \wedge \boldsymbol{b}_{\ell_i^3}\right). \tag{B12}$$

This can be achieved in many ways. For example, with the following local U(3) matrix:

$$U_i = \begin{pmatrix} 0 & 1 & 0 \\ 1 & 0 & 0 \\ 0 & 0 & 1 \end{pmatrix} \tag{B13a}$$

or with the local U(1) transformation

$$\theta_{\ell_i^1} = \theta_{\ell_i^2} = \theta_{\ell_i^3} = \frac{\pi}{3} \tag{B13b}$$

or with the combined action of a local $V_i \in \mathrm{SU}(3)$ and a local U(1) transformation,

$$V_i = \begin{pmatrix} 0 & e^{+\mathrm{i}\pi/3} & 0 \\ e^{+\mathrm{i}\pi/3} & 0 & 0 \\ 0 & 0 & e^{+\mathrm{i}\pi/3} \end{pmatrix},$$

$$\theta_{\ell_i^1} = \theta_{\ell_i^2} = \theta_{\ell_i^3} = -\frac{\pi}{3}. \tag{B13c}$$

Notice that we can equivalently define the vectors $\boldsymbol{b}_\ell$ in $\mathbb{R}^3$. In this case, the cancellation of color-mismatching configuration terms is due to vanishing odd Gaussian integrals over real variables. The resulting $\mathrm{O}(3) = \mathbb{Z}_2 \times \mathrm{SO}(3)$ symmetry is indeed a subgroup of $\mathrm{U}(3) = \mathrm{U}(1) \times \mathrm{SU}(3)$ obtained above.

It is interesting to remark how the use of the Levi-Civita tensor, which plays a key role in uncovering the hidden symmetry, is a nontrivial choice in Eq. (B5). Indeed, all we need there is to forbid the same color to appear twice at the same vertex. This is naturally achieved by a tensor corresponding to the absolute value of the totally antisymmetric tensor $|\varepsilon_{\alpha\beta\gamma}|$. Using instead the Levi-Civita tensor results in the introduction of spurious negative signs associated to some of the vertices, which ought to be dealt with carefully, as in our discussion above. The Levi-Civita tensor (and not its absolute value) is, however, key to the hidden SU(3) symmetry.

From the symmetry of this construction, one sees that the height representation [4] takes values in the weight lattice of SU(3). The global SU(3) symmetry on the lattice is then promoted to a current algebra symmetry in the continuum, namely that of the well-known Frenkel-Kac scalar-field representation of "simply laced" affine Lie algebras. The two currents of the Cartan subalgebra are $i\partial h_1$ and $i\partial h_2$ (where h_1 and h_2 are the two components of the scalar field); whereas the six currents associated with the roots $\vec{G}$ of the reciprocal lattice are the vertices $\exp(\pm i\vec{G}\cdot\vec{h})$. The normalization due to the current Lie algebra relations fixes the value of the level $k = 1$ as a byproduct. Similarly to the better known SU(2) case, one thus obtains that the three coloring model is described in the continuum limit by an $\mathrm{SU}(3)_{k=1}$ CFT. (A similar argument was later derived and published independently by Kondev *et al.* [5].)

We close by noting that the introduction of generic interactions between the chirality spins explicitly breaks the SU(3) symmetry—which is the case e.g., for the nearest neighbor interactions in Sec. II A. Indeed, in order to identify the Ising spin at a given site of the honeycomb lattice, we seek a local combination of the $\bar{b}$'s and b's that is a U(1) singlet and that picks up a sign under odd permutations of the three colors around the site.

For instance, the quantity

$$\det\left(\boldsymbol{b}_{\ell_i^1}, \boldsymbol{b}_{\ell_i^2}, \boldsymbol{b}_{\ell_i^3}\right) \mathrm{per}\left(\bar{\boldsymbol{b}}_{\ell_i^1}, \bar{\boldsymbol{b}}_{\ell_i^2}, \bar{\boldsymbol{b}}_{\ell_i^3}\right), \tag{B14a}$$

for $i \in A$ and

$$\mathrm{per}\left(\boldsymbol{b}_{\ell_j^1}, \boldsymbol{b}_{\ell_j^2}, \boldsymbol{b}_{\ell_j^3}\right) \det\left(\bar{\boldsymbol{b}}_{\ell_j^1}, \bar{\boldsymbol{b}}_{\ell_j^2}, \bar{\boldsymbol{b}}_{\ell_j^3}\right), \tag{B14b}$$

for $j \in B$, satisfies both conditions. However, if we recall that a permanent can be expressed as

$$\mathrm{per}\,(\boldsymbol{A}, \boldsymbol{B}, \boldsymbol{C}) = \sum_{\alpha=1}^{3}\sum_{\beta=1}^{3}\sum_{\gamma=1}^{3} |\epsilon_{\alpha\beta\gamma}| A^\alpha B^\beta C^\gamma, \tag{B15}$$

we immediately recognize that the SU(3) symmetry is lost once we introduce such term in the partition function.

[1] R. J. Baxter, J. Math. Phys. **11**, 784 (1970).
[2] N. Y. Reshetikhin, J. Phys. A **24**, 2387 (1991).
[3] The very elegant argument put forward by N. Read was never published and we report it for completeness in Appendix B, with his kind permission.
[4] D. A. Huse and A. D. Rutenberg, Phys. Rev. B **45**, 7536 (1992).
[5] J. Kondev and C. L. Henley, Nucl. Phys. B **464**, 540 (1996); J. Kondev, J. de Gier, and B. Nienhuis, J. Phys. A **29**, 6489 (1996).
[6] J. E. Moore and D.-H. Lee, Phys. Rev. B **69**, 104511 (2004).
[7] C. Castelnovo, P. Pujol, and C. Chamon, Phys. Rev. B **69**, 104529 (2004).
[8] M. J. Higgins, Y. Xiao, S. Bhattacharya, P. M. Chaikin, S. Sethuraman, R. Bojko, and D. Spencer, Phys. Rev. B **61**, R894(R) (2000).
[9] K. Park and D. A. Huse, Phys. Rev. B **64**, 134522 (2001).
[10] Y. Xiao, D. A. Huse, P. M. Chaikin, M. J. Higgins, S. Bhattacharya, and D. Spencer, Phys. Rev. B **65**, 214503 (2002).
[11] B. Chakraborty, D. Das, and J. Kondev, Eur. Phys. J. E **9**, 227 (2002).
[12] B. Chakraborty, D. Das, and J. Kondev, Physica A **318**, 23 (2003).
[13] D. Das, J. Kondev, and B. Chakraborty, Europhys. Lett. **61**, 506 (2003).
[14] C. Castelnovo, C. Chamon, C. Mudry, and P. Pujol, Phys. Rev. B **73**, 144411 (2006).
[15] J. L. Jacobsen and F. Alet, Phys. Rev. Lett. **102**, 145702 (2009).
[16] P. Lecheminant, A. O. Gogolin, and A. A. Nersesyan, Nucl. Phys. B **639**, 502 (2002).
[17] M. Arlego, D. C. Cabra, J. E. Drut, and M. D. Grynberg, Phys. Rev. B **67**, 144426 (2003).
[18] These effective Ising spins are *not* to be confused with the chirality spins introduced earlier. Note in particular that, by construction, a fully AFM configuration of the chirality spins corresponds to a fully FM configuration of the effective spins on the triangular lattice. Whereas this may seem an annoying source of confusion at the moment, we see that this choice for the effective spins is in fact of great help in understanding the behavior of the system along the $x_A = x_B \to -1$ line.

[19] H. N. V. Temperley, Proc. Roy. Soc. A **202**, 202 (1950); R. M. F. Houtappel, Physica **16**, 425 (1950); G. H. Wannier, Phys. Rev. **79**, 357 (1950).

[20] B. Nienhuis, Two-dimensional critical phenomena and the Coulomb Gas, in *Phase Transitions and Critical Phenomena*, Vol. 11, edited by C. Domb, M. Green, and J. L. Lebowitz (Academic Press, London, 1987).

[21] C. Castelnovo, C. Chamon, C. Mudry, and P. Pujol, Ann. Phys. **322**, 903 (2007).

[22] The reader familiar with the height mapping discussed in Ref. [5] may recall that any two-color loop configurations in the three coloring model can be seen as equal height contours in one of the two height components (for an appropriate choice of the height mapping vectors). AFM correlations between loops imply that if the height goes up crossing one loop in a given direction, then it must go down crossing the adjacent loop in the same direction. A few drawings should suffice to convince oneself that it is always possible to consistently construct a surface compatible with the contour loops, given this recipe. On the other hand, FM interactions require the same height change to occur crossing adjacent loops in the same direction and this condition cannot be always satisfied by a single valued surface (consider for instance a hexagon with three adjacent loops). The only loop configurations where FM correlations are not frustrated need to have all the loops parallel to each other and therefore winding around the system (there are clearly $\sim 2^L$ such configurations).

[23] F. Alet, Y. Ikhlef, J. L. Jacobsen, G. Misguich, and V. Pasquier, Phys. Rev. E **74**, 041124 (2006).

[24] S. Papanikolaou, E. Luijten, and E. Fradkin, Phys. Rev. B **76**, 134514 (2007).

[25] H. W. J. Blöte, J. L. Cardy, and M. P. Nightingale, Phys. Rev. Lett. **56**, 742 (1986); I. Affleck, *ibid.* **56**, 746 (1986).

[26] H. W. J. Blöte and B. Nienhuis, Phys. Rev. Lett. **72**, 1372 (1994).

[27] P. C. Verpoort, J. Simmons, and C. Castelnovo, Cambridge University Apollo Repository, https://doi.org/10.17863/CAM.24358 (2018).

[28] Note that τ is no longer a symmetric matrix, and also not necessarily positive semi-definite. Nonetheless, for the eigenvector v with largest (positive) eigenvalue Λ_0^T of matrix T, the vectors $w_\pm = \sqrt{\Lambda_0^T}\, v \pm \tau v$ can be constructed, which are eigenvectors of τ with eigenvalues $\pm\sqrt{\Lambda_0^T}$. Also, all other eigenvalues of τ have to be smaller in magnitude than $\sqrt{\Lambda_0^T}$. Hence, the largest eigenvalue of τ must be $\Lambda_0^\tau = \sqrt{\Lambda_0^T}$.

[29] O. Cépas, Phys. Rev. B **95**, 064405 (2017).